Circumstellar Disk Astrochemistry

Student: Johanna Teske
American University Advisor: Dr. Nathan Harshman
DTM Advisors: Dr. Alycia Weinberger & Dr. Aki Roberge

Fall 2007—Spring 2008
Graduating with Honors in Physics

Circumstellar Disk Astrochemistry

Johanna Teske[1] & Alycia Weinberger[2] & Aki Roberge[3]

ABSTRACT

One of the most exciting and promising fields in modern astronomy is the detection and classification of extrasolar planetary systems. The processes that produce other worlds begin early the in the life of the host star with formation of an equatorial disk of gas and dust to stabilize the rapidly contracting and rotating protostar. Planetary studies rely heavily on these circumstellar disks, which are found at various stages of stellar life and ultimately make up the diverse range of planets we see today. There are important stages of disk evolution that are not well understood; this Capstone focuses on debris disks, representing an intermediate stage between gas-rich protoplanetary disks and established planetary systems. To further understand the complex interaction of gas and dust in these disks, the optical spectra of A-shell stars were examined via measurement of absorption line strength and radial velocity to characterize their circumstellar material and diagnose why some stars show little evidence for a dust component, while others have significant infrared excess.

1. Introduction

In modern astronomy, one of the most exciting fields attracting scientists from across disciplines is the detection and characterization of extrasolar planets, unique and exotic worlds that have been postulated to exist for centuries but only recently confirmed. The rate of discovery of "alien" worlds has accelerated tremendously within the last decade alone, thanks in great part to the enhanced technologies and observational facilities, and shows no sign of slowing down. Studies of extrasolar planets—their orbital properties, chemical/physical compositions, atmospheres, and environments—is important not only for understanding the diversity of our galaxy and universe, and the possibility of life elsewhere, but also for contextualizing the formation and evolution of our own Solar System. For example, how did water arise on Earth? By examining the temperature gradients across a range of extrasolar systems, we can create a map of water location and transportation, what species of it are found (ice, liquid, gas) and when, and perhaps determine if it could have formed close to our Sun or whether it came from the environs of another star. What about the formation of the gaseous planets—is this a common occurrence, i.e., are more extrasolar planets gaseous versus rocky/terrestrial? What initially starts the formation of a planet? Extrasolar planetary study in all aspects can help answer these and a multitude of other questions, as well as inspire new inquiries into our own origins.

While observing mature planets has been successful, it is equally if not more important to study the evolution leading up to this stage. Viewing the end-product alone cannot explain why certain characteristics are observed, or how they might vary across time, distance, composition of the host star, etc. The processes

---

[1]Dept. of Physics, American University, Washington, DC 20016. Email jteske@hotmail.com.

[2]Dept. of Terrestrial Magnetism, Carnegie Institution of Washington, Washington, DC, 20015

[3]Goddard Space Flight Center, Greenbelt, Maryland, 20771

that produce these other worlds begin very early the life of the host star, which is formed from the collapse of a cloud of molecular gas and dust in the interstellar medium (ISM). It is currently not well understood what causes the collapse (although a popular explanation is the influence of a near-by supernova event), but once material starts to fall inwards, it begins to heat up. To conserve angular momentum, the system also begins to spin, and much like a spinning top or a piece of pizza dough, its material stabilizes with the formation of an equatorial disk around the core of the rotating "baby" protostar. Once the star shrinks to a critical radius, it is hot enough to ignite hydrogen fusion, which will eventually lead to its start on the standard main sequence of stellar evolution (once hydrogen fusion becomes the dominant mechanism of energy production). The equatorial disk goes from opaque and nebulous to more resolved and "dusty" as more material clumps together and/or falls inward towards the star; at first most is accreted onto the protostar, but soon a distinct *circumstellar disk* of rotating material is observed. It is during this circumstellar disk stage that planet formation is believed to occur. There is a plentiful supply of gas and dust that continues to be replenished by the ISM, and collisions and evaporation/heating around the star transport and alter the size and type of small solid bodies (planetesimals) that can condense. As the star heats, it continues to evaporate both old and newly coagulated material close-by to it (within several AU). Eventually new planetesimal growth slows, and ceases; the planets of the system have (at least) mostly formed, although objects may still be colliding with each other to form craters and asteroid, like those we see on our Solar System planets and satellites (e.g., our own Moon).

1.1. Disks

Observation of the Solar System agrees well with this disk explanation, as all of our planets orbit the Sun in roughly the same plane, and we still have remnants of planetesimals in the asteroid and Kuiper Belts. Beginning in the 1960s, excess infrared (IR) emission observed toward young stars was attributed to dust particles, which absorb the ultraviolet and optical light given off by a star and reradiate in the infrared wavelengths. The most popular hypothesis for roughly two decades was that young stars were surrounded by spherical "shells" of material. The fascination with disks continued through the 1970s, when they were used to explain masers (Reid et al. 1977), stellar polarization (Bastien 1982, Breger 1978), silicate emission from planetary nebulae (Kwok 1980), and as astronomers realized circumstellar *shells* were more likely nonspherical, resembling disks more closely (e.g. Strom et al. 1972, Smith & Terrile 1984). However, confirmation of circumstellar disks around *main sequence* stars like our Sun did not come until the launch of the *Infrared Astronomical Satellite* (IRAS) in 1983 and its subsequent detection of dusty disks around Vega, Beta Pictoris, and Fomalhaut (Aumann 1985). These specific objects have continued to be observed and remain prominent in the literature, but have been followed by further detection of disks around stars of types A, F, G, K, and M (e.g. Rieke et al. 2005, Spangler et al. 2001, Meyer et al. 2008, Gautier et al. 2007), ranging in age, temperature, and luminosity. Dust still present in a system is exciting because it indicates planet formation recently/may still be taking place, and in a wide range of environments. Now disks are generally categorized by their *fractional infrared luminosity*, or the amount of infrared light detected in relation to the light detected or expected from the star. This diagnostic, called *tau*, is highest in the youngest stellar systems and appears to decrease as the grains of dust continue to coagulate (Spangler et al. 2001); once they reach sizes of a more than a few microns, dust particles are no longer observed in the IR (Natta et al. 2007). Disks with higher L_{IR}/L_* ($\sim$ 0.3) are labeled as protoplanetary or primordial disks and still house the original gas and dust of the molecular cloud collapse (from examples in Weinberger et al. 2002). Observations of protoplanetary disks have revealed their contained material orbits at distances roughly between 0.1 and 30 AU (although perhaps as great as 1000 AU) from their host stars, and lasts for approximately 10 Myr after initial cloud collapse (Silverstone et al. 2006). The gas-to-dust (by mass) ratio in protoplanetary disks is initially similar to the ISM ratio of $\sim$100 (Hildebrand 1983). This is followed by a short, rare phase known as transitional disks, intermediary between a full disk accreting onto a protostar and a highly dissipated disk in which accretion has generally ceased (Skrutskie et al. 1990). Observations of stars with short-lived ($\sim 10^5$ yr, i.e. McCabe et al. 2006) transitional disks have shown clearing of an inner hole around the host star, indicative of its enhanced evolution and perhaps transportation of dust and gas further out in the disk. When material is further from the star, it can condense and/or freeze to form larger solid bodies and ices of varying composition, again dependent on the original environment of the star and how massive the star has become. Once the fractional luminosity reaches $\sim 10^{-5} - 10^{-3}$ (Backman & Paresce 1993), the gas-to-dust ratio is reversed and the disk has reached the debris stage. In debris disks, dust masses are generally under an Earth mass ($\sim 3 \times 10^{-6}$ M_{sun}; the minimum mass required for formation of planetary system like our own is roughly 1×10^3 M_{sun} (Telesco 2000)). At this point, material observed originates mostly from the interactions of previously formed/coagulated, secondary particles (e.g. asteroids and comets)—they smash into each other, evaporate when they approach too near the host star, and can be dissociated into individual atomic/molecular species by the ultraviolet radiation of the host star. Debris disks are the longest stage (our Solar System still has a debris disk), and can last through the main sequence to remerge as a diagnostic tool for characterizing what has happened during the life of the star. This circumstellar disk phase is the focus of the present work.

Because of the lower gas to dust in these older disks (and the fact that it was the dust caused their original detection), observations and study of the *gas* in debris disks has not been as wide-spread; many studies of debris disks have focused on the observation and evolution of their dust. Gas is more difficult to "see" because it is far less abundant than the dust; Zuckerman et al. (1995) noted that their observations of molecular gas around Sun-aged stars implied significantly lower gas masses than inferred from dust observations. Furthermore, the most prominent gas species, H_2, has electronic transitions that are confined to the UV and hardly observable from the ground, and its abundance in some debris disks is weak (Roberge et al. 2005). This presents a serious problem, since even simple models of dust growth and transport have to take into account the dust-to-gas interaction to be relevant. Gas motion and pressure controls where the dust travels and settles, depending on the size of the dust grains and their intrinsic velcoity—smaller grains usually orbit farther from the center of the disk (Takeuchi & Artymowicz 2001). Thus gas plays a large role in cleared-out zones and particle belts, the formation of comets and asteroids, the location of resonances in the disk, and perhaps the formation of rings around extrasolar planets (Zuckerman 2001). Furthermore, the gas is diagnostic of temperature, radiation pressure from the star, location of the "snow" line of various species, and the chemical composition of the solid material that may have evaporated. Most obviously, any residual gas in the system also contributes to and constrains the timescale for giant gas planet formation (like our Jupiter and Saturn) (Zuckerman 2001, Pascucci et al. 2006). Previous observations of debris disks in the UV and optical—β Pictoris (e.g. Lagrange et al. 1998), 51 Ophiuchi (e.g. Roberge et al. 2002), σ Herculis (Chen & Jura 2003), and HD 32297 (Redfield 2007)—have shown the presence of atomic gas, but the sample needs to be increased. It is from these atomic transitions that the most information about debris disks can be gleaned. The goal of this paper is to aid in understanding the gas component of debris disks and its relationship to the dust by both increasing the number of debris disk-gas detections and helping to identify and explain the gas. In addition, we hope to use the composition of the gas itself to characterize the secondary solid material (planetesimals, comets) from which it is most likely vaporized, and "map" the temperature scales across the disk.

Fig. 1.— Canonical circumstellar disk β Pictoris observed in the infrared by Jean-Luc Beuzit et al., 1997, Grenoble Observatory, European Southern Observatory

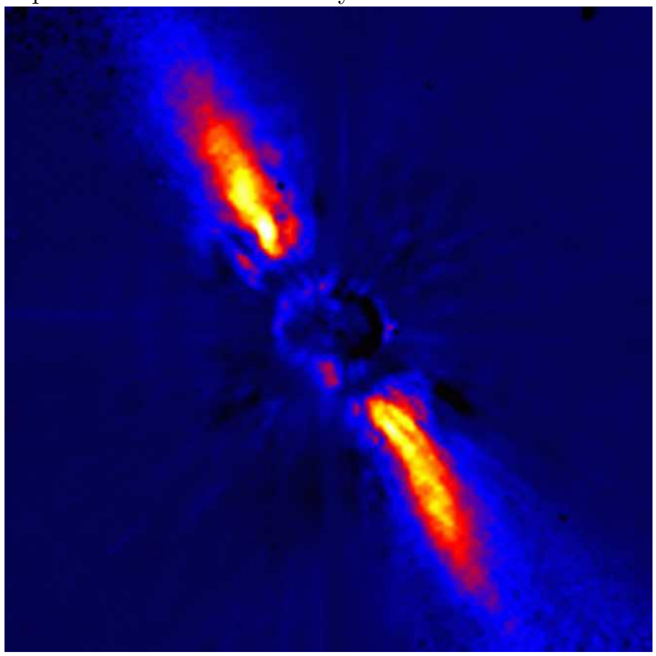

1.2. Shell Stars

A class of peculiar *shell* stars could be a valuable key in the detection of edge-on debris disks containing gas. Struve (1932) and Morgan (1932) first recognized A- and F-type shell stars by two sets of lines, one broad and one sharp, which they attributed to a rapidly rotating underlying star surrounded by an outer shell of gas. Abt and Moyd (1973) performed the first in-depth study of shell stars, though other examples were found by Andersen and Nordström (1977), Cowley and Hiltner (1968), Greenstein (1953), and Slettebak (1963, 1975). These stars' spectra show very narrow absorption lines, which are thought to arise from atomic ground states and/or metastable levels in line-of-sight circumstellar gas at the velocity of the star (Slettebak 1982). Abt and Moyd differentiated the shell stars as having absorption lines at Ca II H and K, Ti II 3685, 3759, 3761, and possibly 3900 and 3915 Å, and Fe II 4233 and 4549 Å. Andrillat et al. (1983) noted that when the redder Ti II and Fe II lines are present, the other lines are seen, but if the Ca II lines are absent, no other shell characteristic lines are observed. Most stars classified as shell-type are B- or A-type (at the high temperature, mass, and luminosity end of the stellar classification scheme), probably because they are bright enough in the optical and UV for detection of weak narrow absorption lines at the bottom of any strong photospeheric lines (and because they lack many narrow photospheric lines). In some cases the lines come from interstellar instead of circumstellar material, but since the gas is detected at the velocity of the target star, this is unlikely. Also, the detected absorption lines are usually stronger than can be explained by interstellar gas alone (Abt & Moyd 1973). From Abt and Moyd's original sample, the shell spectra were not seen in program stars with $v \sin i \leq 175$ kms^{-1}, though they would have been distinguishable from atmospheric lines even in stars with moderate rotational velocities. This velocity limit was increased by Abt et al. (1997) to 200 kms^{-1} with a study of 54 similar types of stars having 90 kms^{-1} $\leq$ $v \sin i \leq 200$ kms^{-1} that displayed no gaseous shell features. That the projected rotational velocities of shell stars exceed those of non-shell A-stars demonstrates that the shells are equatorial versus spherical, and that the gas is more likely to be observed when the line-of-sight intersects the rotational plane of the star (e.g. Holweger, Hempel, & Kamp 1999). (This only strengthens the case for a circumstellar rather than interstellar source of most shell absorption lines.) Abt (2008) thus suggests shell stars should actually be called "disk stars". Abt and Moyd (1973) ultimately suggested that all rapidly rotating stars have a high probability of becoming shell stars at some point in their lifetime.

Though it is thought that many shell stars are older and rapidly rotating, a recent evaluation (Hauck & Jaschek 2000) of the luminosity classes of 57 shell stars concluded that 40% fell on the main sequence. As of yet, their nature is not well understood, but of the 23 main sequence stars in the Hauck and Jaschek sample, 6 have been confirmed as young circumstellar disk stars (MWC 480, β Pic, HD 97048, HD 139614, HD 163296, & HD 179218). Also, another member of the Hauck & Jaschek sample (HD 144667) is an accreting Herbig Ae star (still-contracting, pre-MS A or B star) that very likely has a protoplanetary disk (e.g. Garcia Lopez et al. 2006). Thus, at the start of this work, while no systematic survey for dust around shell stars has been attempted, the fraction of main sequence shell star systems harboring protoplanetary or debris disks appears to be at least 30%. Furthermore, an *Infrared Space Observatory* (ISO) survey of 84 main sequence stars of various ages within 42 pc found disks around 17% of the sample (Habing et al. 2001), implying that the disk fraction for main sequence shell stars ($\geq$ 22%) may be higher than for ordinary main sequence stars.

1.3. Previous Work

The work outlined in this paper builds upon the manuscript *Debris Disks Around Nearby Stars with Circumstellar Gas* (Roberge & Weinberger 2008), presenting a detailed survey with the Multiband Imaging Photometer (MIPS) on the *Spitzer Space Telescope* for infrared excess emission (at 24 and 70 μm) from 16 nearby main sequence shell stars. Roberge and Weinberger searched for the characteristic excess emission from dust in circumstellar disks with the goal of increasing the number of known debris disk systems in which gas detection was also significant.

Target selection for that paper was based on the 57 shell stars in the Hauck & Jaschek (2000) sample that most likely included young disk systems with circumstellar gas and dust. Only stars with luminosity class V (23 stars) were included to focus the sample on main sequence systems (as opposed to those likely to be evolved mass-losing stars). The six systems already known to have disks were eliminated, as were ordinary stars that may have originally been misclassified as shell stars due to their large distance (making their spectra more likely contaminated by material along the line-of-sight of the observer). Additionally, four shell stars showing narrow, time-variable absorption features in their spectra (confirming the line-of-sight gas as circumstellar) were added to the list: HD 42111 (Lecavelier des Etangs et al. 1997), HD 50241 (Hempel & Schmitt 2003), HD 148283 (Grady et al. 1996), and HD 217782 (Cheng & Neff 2003).

Roberge and Weinberger's study was successful, finding 4 out of 16 surveyed stars with excess emission at 24 and 70 μm that signified debris disk candidacy. This increased the disk fraction among the Hauck and Jasheck (2000) main sequence shell stars to at least 11 out of 23 (48% $\pm$ 14%). The study demonstrated that surveys for shell stars in the optical and IR is an effective way of finding protoplanetary and debris disks. Interestingly, the four stars with claims for variable circumstellar gas that were added to the Hauck and Jaschek stars did *not* display any excess IR emission, in agreement with Redfield et al. (2007)'s *Spitzer* observations of three other stars with variable circumstellar gas. These stars represent a mysterious category of main sequence shell stars that show time-variable, narrow absorption lines yet no obvious dust component. This poses the question, why do some shell stars show both gas and dust while others show no dust component, and how are these components related? The current paper seeks to help answer this by closely examining the sample used in Roberge and Weinbergert's MIPS survey for gaseous component signatures.

2. Observations

We have obtained optical observations of the sample using the Clay (Magellan II) Telescope at Las Campanas Observatory in Chile, with the Magellan Inamori Kyocera Echelle (MIKE) spectrograph, and using the 2.7 m Harlan J. Smith Telescope at McDonald Observatory with the 2dcoudé cross-dispersed echelle spectrograph. The MIKE data were taken during six nights distributed over three observing runs in March 2007, October 2007, and March 2008, and the McDonald data were taken over three nights in November 2007. On March 9-10, 2007 the weather was clear at sunset with low haze and no wind, and remained clear during March 10-11 observing. The seeing[4] on March 9-10, 2007 ranged from 0.43-1.1" and on March 10-11, 2007 ranged from 0.5-1". The signal-to-noise (S/N) for March 10-11 was about 70-140, except $<$ 3700, when it was lower around 40. In October 2007 the seeing ranged from 0.4-1.7" on October 24, 2007, from 0.5-2.0" on October 25, from 0.7-1.5" on October 26, and from 0.5-1.4" on October 27. The S/N for October 24 and 25 was $>$ 100, reaching 300 near the middle of the spectra, for $>$4000 Å, and decreased to 20-175 for $<$ 4000 Å (especially towards the blue edge of the spectra). It was slightly worse for October 27. In November 2007 the seeing was of poorer quality and the nights were slighly cloudy. The seeing on March 21, 2008 ranged from 0.5-0.9", was around 0.7" on March 22, and ranged from 0.9-2" on 23 March; the weather was clear all three nights. The S/N for March 2008 was generally $\geq$100, at times reaching almost 400, at $>$4000 Å, but decreased to an average of 50-100 for bluer wavelengths; the best S/N was on March 22. Our spectra have a resolution of $\sim$50,000 (MIKE) and $\sim$60,000 (2dcoudé). The exposure times for each target are listed in Table 10.

In general, spectroscopic observations require some dispersing element such as a diffraction grating or prism to produce the spectrum of stellar light, which is then recorded with a charged-coupled device (CCD) or other type of camera. As explained in *An Introduction to Echelle Spectroscopy*, "the wavelength range covered by this [traditional spectrographs] type of spectrograph is limited by the size of the available image sensors, i.e., CCDs." To optimize the available detector area, an echelle diffraction grating can be used. This grating has lines that are ruled much farther apart than those of an ordinary diffraction grating, giving very high dispersion but a short wavelength range in each order. This grating produces very high resolution observations, but requires the object to be relatively bright in order to fill the slit of the telescope. The orders also overlap at higher wavelengths, so a cross-dispersing element is used to create a gap between adjacent orders. The echelle spectrographs designed for astronomy have overlapping wavelength coverage from one order to the next, at least for the middle orders in the full echellogram; this can be a problem for resolving multiple faint targets in a field of view. (from *An Introduction to Echelle Spectroscopy*[5]).

MIKE is double beam echelle spectrograph (observing in red and blue channels) with complete optical wavelength coverage (320nm–1μm). The full wavelength range of the spectrograph covers 3200–5000 Å (blue) and 4400–10000 Å (red); the blue and red channels are used simultaneously to obtain spectra over these ranges, with only limited wavelength gaps at the reddest orders. (Bernstein et al. 2002) At

---

[4]The term *seeing* in astronomy refers to the quality of observing conditions on a given night due to atmopheric turbulence. The better the seeing, the better the angular resolution that the telescope can achieve, meaning more accurate and resolved observations.

[5]Martin Clayton, 11 December 1996, Starlink Project, online at `http://zuserver2.star.ucl.ac.uk/ mjc/echelle/sg9.htx/sg9.html`

McDonald, the spectrograph is attached at the coudé focus, which is traditionally located away from the moving telescope in another room so that larger attachments (e.g. a high-dispersion spectrograph) can be fitted without interfering with the telescope performance and balance. It has two focal modes—cs23 with resolving power 60,000 and cs21 with resolving power 240,000—and two echelle gratings—10.5 and 15.5 arcsec. Our observations were made in cs23-e2 mode, collecting data across 3400-10900 Å (Tull et al. 1995; `http://hebe.as.utexas.edu/2dcoude/`).

By measuring the strength of absorption lines in the systems due to various atomic gases, we analyzed the composition of their circumstellar material, while also attempting to determine the kinematics of the gas, which can reveal where in the disk it resides. For each shell star target, a control sample of "mini-survey" stars surrounding the target (within 2-3 degrees and 25 pc distance) and with similar interstellar lines of sight were simultaneously observed and analyzed to distinguish circumstellar from interstellar gas. Additionally, we searched for variability in the lines indicative of specific planetesimal evaporation events as are observed in β Pictoris. The full sample is listed in Table 10.

Fig. 2.— Raw MIKE spectrum of HD 50241, prior to pipeline processing.

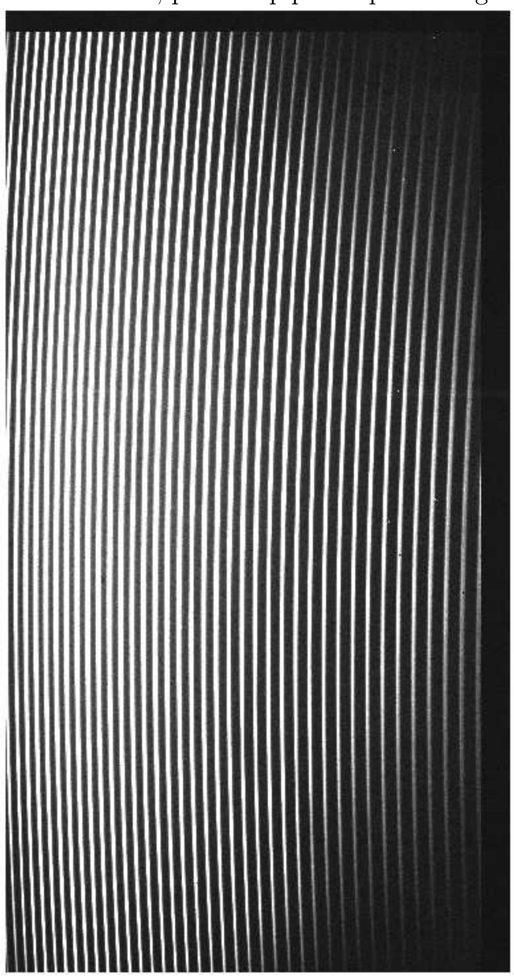

3. Spectral Extraction

To extract the Magellan spectra, we used the analysis pipeline written by Dan Kelson of the Carnegie Observatories specifically for the MIKE instrument. The Python code performed all of the necessary corrections on the raw CCD images to correct for instrumentation effects and prepare the spectra for extraction. The McDonald data required direct (unautomated) reduction using the Image Reduction and Analysis Facility (IRAF, an open-source software used for general reduction and analysis of astronomical data)[6], including:

Trimming subtraction and overscan correction from data, arcs, flat field, and bias frames: This procedure ensures that only the actual spectral information is being analyzed. It removes pixels that are not illuminated by the target (the "overscan" region). Also, the curving of the orders (slits on which the light enters and line absorption/emission features are recorded) is mapped. Arcs refer to frames of a thorium-argon lamp, which burns with a characteristic spectrum. They are used as a reference to calibrate the wavelength scale of the spectra. Biases represent the "pedestal level" read of the CCD—the number of counts recorded for each pixel with zero exposure time and zero actual photons. This comes from the voltage maintained in the camera electronics to bias the semiconductor and keep the signal detected from going negative. (Williams & Ledlow 1998)

Combining the bias frames, flat frames: The flat field is a frame illuminated with some uniform source that is then used to determine the relative sensitivity of the pixels in the system being used. The pixel-to-pixel variations caused by the sensitivity of the detector and any distortion in the light path between the sky and detector are recorded on the flat field frame. For 2-D spectra, like echelle, the two issues must be treated separately. An internal continuum source is used to correct for pixel-to-pixel variations (quartz lamp flats), while a series of twilight sky exposures is used to correct for the optical system distortions (milky sky-flats). All flat field frames are then convolved together to form one flat field frame to be used in subsequent data reduction, as are all the bias frames. (They can also be used individually or convolved based on observing night.)

Normalizing the flat field: Before dividing by the flat-field to remove the sensitivity variations of the instrument, the observed flats must be normalized. The goal of normalization is to create a frame and use it to divide out pixel-to-pixel gain variations across the CCD caused by wavelength-dependent quantum efficiency differences, interference patterns, and dust particles. Applying the flat field directly would distort the object spectra—the pixel values would no longer correspond to the actual observed signal—and could magnify the noise between the orders (since the flat field signal between orders may approach zero). Before the flat field can be normalized, the locations of the individual echelle orders must be mapped on the CCD frames. Initially one of the flat field frames is used to find and size the apertures, set the regions to be used for background subtraction (the continuum), and trace the apertures to make sure the model created fits well. Then this aperture model is tested on one of the target sources and appropriately resized to best fit the data. After normalization, the difference between any pixel value and unity corresponds to the variation from the mean gain (the pixels between the orders are replaced with unit response).

Applying the flat field and bias corrections to the data and arcs

Extracting the spectra: The two-dimensional images of the echelle apertures are transformed into a single intensity versus pixel spectrum for each aperture. The aperture model tailored to the data image

[6]IRAF is distributed by the National Optical Astronomy Observatories, which are operated by the Association of Universities for Research in Astronomy, Inc., under cooperative agreement with the National Science Foundation. More information at `iraf.noao.edu`.

is used, and each extraction can be visually inspected during the extraction procedure for obvious errors. Also extracted are the background and sigma spectra (estimated sigma of each pixel based on the separate variances of the pixels summed). For our analysis of the data frames we set background to "fit" and the profile fitting type to "fit2d"; for the Th-Ar lamps we did not subtract the background. Also, for both data and Th-Ar lamps, we did not use the clean function (automatically detect and replace bad pixels) or weight the spectra.

Fig. 3.— Extracted spectrum from MIKE pipeline.

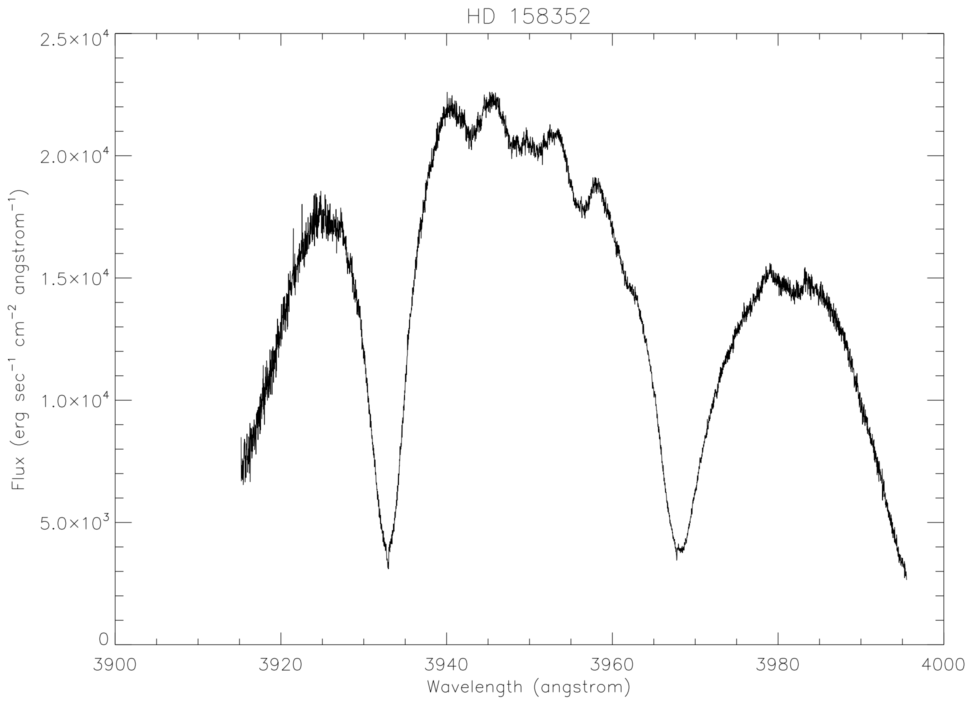

Performing and applying the wavelength calibration: Following these procedures, the echelle spectra must also be wavelength calibrated, using the "arc" lamp frames (which are first added together). To begin, an order is found that has clearly matching lines to a known range of features in a Th-Ar atlas. The lines in the extracted spectrum order are marked manually based on this comparison, and then one moves to higher and lower orders, manually identifying four or more lines in each. A first fit is performed after identifying about twenty lines, roughly determining the offset from the online coordinate list provided by IRAF. The process is repeated multiple times, including identifying more/weaker lines across all of the orders, and then performing fits with more tightly constrained parameters, matching the Th-Ar atlas more closely with each iteration. Each fit attempts to minimize the fitting residuals, which are examined between fits in plots of residuals versus pixel and/or versus wavelength. The fitting function is appropriately modified to remove any waves or structure across the columns (by changing the xorder and yorder parameters). After this dispersion solution is created, it is added to the data header files with `refspectra` and applied to the data with the task `dispcor`.

The specifics of the MIKE pipeline are detailed in the documentation available with the download of the code, at `http://www.ociw.edu/Code/python/kelson/pkgs/` (described in Kelson et al. 2000, Kelson 2003, and Kelson et al. 2006). Briefly, the required files were, as outlined above, milky flat frames (preferably taken

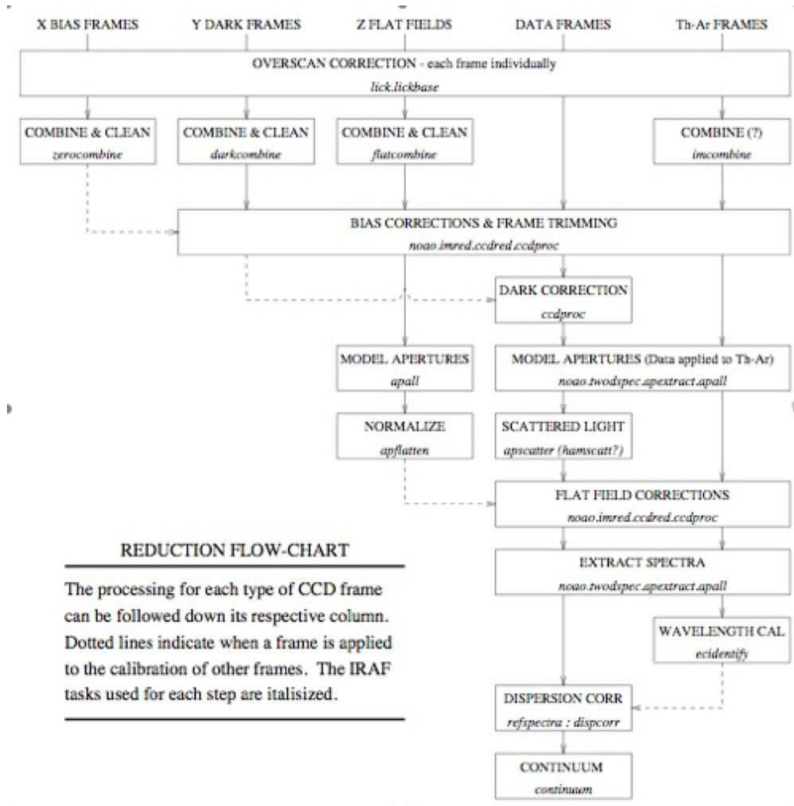

Fig. 4.— Above is a diagram from Introduction to Echelle Data Reduction using the Image Reduction Analysis Facility (Churchill 1995) detailing the complete IRAF reduction procedure and related commands. This documentation was written for the Hamilton spectrograph at Lick Observatory, but was easily generalized for use with our data, although we did not perform all steps of this analysis procedure, leaving out the scattered light correction, flat field normalization and correction application, and the continuum subtraction.

using a hot blue star or quartz lamp), quartz or twilight frames used to locate the order edges and map order curvature, target frames, and lamp frames used to map the line curvature and for wavelength calibration. Before beginning data reduction, the pipeline created a text file comprised of the necessary parameters from the header files[7] of each target including all the files that were saved in the working directory (we broke the directories up by night observed). The OBJECT header key, the identifying label the observer gives each observation, was used to differentiate between the required files—"thar" signified that the file was to be run through analysis as a lamp frame; "milky" signified the file was to be run as a flat field frame; "quartz" signified the file was to be run as a quartz (non-milky) frame for finding order edges.

Next, analysis pipelines (code scripts to generate a new normalized flat field, generate a good reference wavelength solution, and reduce the science target) were generated for each target, in both the red and blue bands. The first execution of the pipeline (either for one target or a group of targets) generated the normalized flat field, which was subsequently used for the rest of the analysis on the appropriate targets (i.e.

[7] A header file contains keywords specifying information about the observation (date, instruments, observer, times, position, etc.) and target (name, filename, position, exposure time).

the combined red flats were used on the red targets). As the individual pipelines ran, each stage generated an empty file denoting completion of that stage, recording which steps remained to be completed. The end product of running all the pipeline commands was a cubed "multispec" FITS file for each target, containing for every order the:

1. sum of the sky over the extraction aperture
2. sum of the object over the extraction aperture
3. expected noise from the sum of the object and sky plus the read noise
4. signal-to-noise spectrum (per pixel)
5. sum of the lamp spectrum over the extraction aperture (only from first lamp exposure)
6. flattened-flat (blaze)
7. spectra divided by the flattened-flat

To "de-cube" these files, we used an IDL program `split_cube` to split the multispec file into its components (numbered 0-6). In subsequent examination of the spectra, the `_multi_2.fits` files were used as the error and the`_multi_6.fits` files were used as the final, good spectra.

4. Analysis and Results

4.1. Radial Velocity Determination

In order to correctly locate and measure the wavelengths in each spectrum, the radial velocity of the star was needed to determine the appropriate shift in angstroms. For many of our target and comparison stars, radial velocity values were not readily available, and had to be determined based on the spectra that we obtained. The IRAF task `xcsao` is the main tool we used to cross-correlated our spectra with models (created with velocity zero) to determine the velocity dispersion. Before running `xcsao`, the barycentric velocity (earth relative to the Solar System center of mass) and heliocentric velocity (earth relative to the sun) corrections had to be set in each spectrum's header file (using the `bcvcorr` task). When a spectrum is input into `xcsao`, the continuum (and, optionally, emission lines) is divided out of the object spectrum using input parameters (function, order, lower and upper rejection limits, and iterations) or a manual curve fit. After both object and template spectra are apodized (tapered at each end for a fraction of the entire spectrum) they are cross-correlated and normalized using the highest correlation peak between the velocities, with therequired height of the peak set by the user. The shift is calculated by fitting a parabola (or similar function) to the portion of the peak above a user-defined fraction (e.g., 0.8) of the maximum of that peak. We varied the template spectra by effective temperature, vsini (projected rotational velocity of the star), and log(g) (surface gravity), constraining what templates we used to correlate best with each spectrum based on the known properties of the target star.

In order to be able to use this procedure with the MIKE pipeline data and the templates created with SPECTRUM[8] and the LTE ATLAS9 model[9] (t09000 templates) or Catelli-Kurucz model atompshere (teff9000 templates) with solar metallicity[10], the former had to be order-merged so that a large enough sample of lines were available in the object spectrum to compare to the model. (Before combining the orders, only a few or no absorption lines were able to be cross-correlated with the model spectrum because it performed a fit over each order individually, leading to very poor fits and incorrect radial velocities measurements.) To merge the orders, first the IRAF task `continuum` was used to interactively fit (varying function order if necessary) a one dimensional function (spline3) to the continuum of the spectrum and then divide that into the spectrum. This continuum was then used along with manually-set wavelength limits for each order, to merge the orders of the spectrum file together into a single spectrum (using the `pymbcombine` program written by Alceste Bonanos). This was then easily compared to models using `xcsao` as detailed above.

Fig. 5.— Order-merged, continuum normalized spectrum.

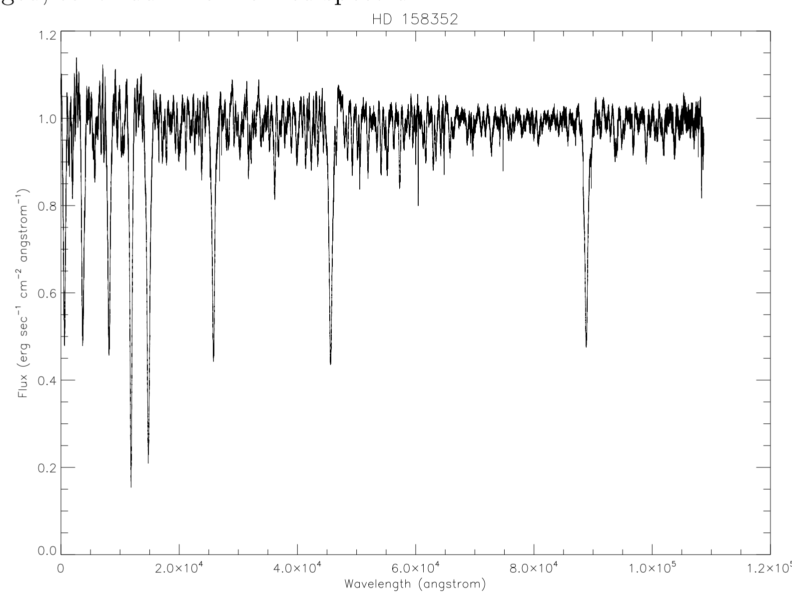

To test this procedure, targets with radial velocities available from the Set of Identifiers, Measurements, and Bibliography for Astronomical Database (SIMBAD4, 1.083-28-April-2008)[11] were used—HD102870 and HD76932 (the latter being a radial velocity standard taken in March 2007)—and produced radial velocity values that corresponded to those previously determined (Evans 1967). The values obtained are listed in Tables 1 and 2. HD 102870, as an F9V star, can be expected to have an effective temperature of $\sim$ 6000 K and has a small vsini ($\sim$ 3)[12]; thus the coolest models with smaller vsini values gave better fits. Similarly, HD 76932 can be expected to have an effective temperature of $\sim$ 5800 K and also has a small vsini; the fit values below match accordingly.

---

[8]SPECTRUM developed by R. O. Gray, `http://www.phys.appstate.edu/spectrum/detail.html`

[9]Kurucz, R. 1993, ATLAS9 Stellar Atmosphere Programs and 2 km/s grid. Kurucz CD-ROM No. 13. Cambridge, Mass.: Smithsonian Astrophysical Observatory

[10]`http://kurucz.harvard.edu/grids/gridP00aODFNEW/ap00k0odfnew.dat`

[11]More information at `simbad.u-strasbg.fr./simbad`

[12]Bernacca, P.L. & Perinotto, M. 1970, Contr. Oss. Astrof. Padova in Asiago, 239, 1B

Table 1. Radial Velocity Determination, HD 102870

Known Radial Velocity = 4.6 ±0.9 kms^{-1} Model[1]	Peak Height	Radial Velocity (kms^{-1})
t09000g40v2r10.fits	0.279	4.18
t09000g40v2r100.fits	0.172	-2.925
t09000g40v2r110.fits	0.169	-4.499
t09000g40v2r120.fits	0.166	-6.249
t09000g40v2r130.fits	0.164	-7.826
t09000g40v2r140.fits	0.162	-9.401
t09000g40v2r150.fits	0.16	-11.065
t09000g40v2r160.fits	0.158	-12.434
t09000g40v2r170.fits	0.156	-14.174
t09000g40v2r180.fits	0.155	-15.426
t09000g40v2r190.fits	0.154	-16.811
t010000g30v2r10.fits	0.275	3.349
t010000g35v2r10.fits	0.251	3.914
t010000g40v2r10.fits	0.224	4.019
t010000g45v2r10.fits	0.2	4.124
t010000g50v2r10.fits	0.188	4.192
t08000g30v2r10.fits	0.436	4.162
t08000g35v2r10.fits	0.431	4.191
t08000g40v2r10.fits	0.436	4.215
t08000g45v2r10.fits	0.446	4.236
t08000g50v2r10.fits	0.454	4.255
t08500g30v2r10.fits	0.362	4.112
t08500g35v2r10.fits	0.349	4.412
t08500g40v2r10.fits	0.342	4.2
t08500g45v2r10.fits	0.349	4.229
t08500g50v2r10.fits	0.36	4.505
t09000g30v2r10.fits	0.32	4.042
t09000g35v2r10.fits	0.296	4.114
t09000g40v2r10.fits	0.279	4.18
t09000g45v2r10.fits	0.271	4.222
t09000g50v2r10.fits	0.272	4.255
t09500g30v2r10.fits	0.294	3.944
t09500g35v2r10.fits	0.267	4.029
t09500g40v2r10.fits	0.244	4.129
t09500g45v2r10.fits	0.227	4.191
t09500g50v2r10.fits	0.222	4.238

[1]The model names are constructed as follows: 't09000' or 'teff9000' = T_{eff} of 9000 K, 'g40' or '_g4.0' = log(g) of 4.0, 'v2r10' or 'v10' = 10 kms^{-1} project rotational velocity

Table 2. Radial Velocity Determination, HD 76932

Known Radial Velocity = 120.8 ±0.9 kms^{-1} Model[1]	Peak Height	Radial Velocity (kms^{-1})
teff7500_g3.5_v10.fits	0.483	119.697
teff7500_g3.5_v100.fits	0.270	119.386
teff7500_g3.5_v200.fits	0.226	116.484
t08000g30v2r10.fits	0.360	120.051
t08000g30v2r20.fits	0.322	120.250
t08000g30v2r30.fits	0.291	120.345
t08000g30v2r40.fits	0.271	120.498
t08000g30v2r50.fits	0.257	120.250
t08000g30v2r60.fits	0.245	119.864
t08000g30v2r70.fits	0.235	119.420
t08000g35v2r10.fits	0.356	120.057
t08000g35v2r20.fits	0.318	120.259
t08000g35v2r30.fits	0.287	120.364
t08000g35v2r40.fits	0.266	120.533
t08000g35v2r50.fits	0.250	120.392
t08000g35v2r60.fits	0.239	119.957
t08000g35v2r70.fits	0.228	119.551
t08000g40v2r10.fits	0.364	120.068
t08000g40v2r20.fits	0.326	120.264
t08000g40v2r30.fits	0.294	120.352
t08000g40v2r40.fits	0.273	120.489
t08000g40v2r50.fits	0.258	120.245
t08000g40v2r60.fits	0.245	119.868
t08000g40v2r70.fits	0.234	119.446
t08000g45v2r10.fits	0.379	119.794
t08000g45v2r20.fits	0.341	120.267
t08000g45v2r30.fits	0.309	120.426
t08000g45v2r40.fits	0.287	120.416
t08000g45v2r50.fits	0.270	120.134
t08000g45v2r60.fits	0.258	119.803
t08000g45v2r70.fits	0.247	119.247
t08000g50v2r10.fits	0.390	119.807
t08000g50v2r20.fits	0.353	120.282
t08000g50v2r30.fits	0.321	120.441
t08000g50v2r40.fits	0.298	120.448
t08000g50v2r50.fits	0.281	120.205
t08000g50v2r60.fits	0.268	119.924
t08000g50v2r70.fits	0.257	119.401

[1]The model names are constructed as follows: 't09000' or 'teff9000' = T_{eff} of 9000 K, 'g40' or '_g4.0' = log(g) of 4.0, 'v2r10' or 'v10' = 10 kms^{-1} project rotational velocity

4.2. Finding and Measuring Absorption Lines

The analysis can next be broken up into two approaches. The first, preliminary approach involved manipulating previously written IDL programs to automatically (non-manually) scan through the MIKE pipeline-generated spectra (and errors) for specific wavelengths and calculate the equivalent widths of those absorption lines. Equivalent width is a measurement of the strength of a spectral line; it is the width of a rectangle centered on a specific wavelength that, on a plot of intensity against wavelength, has the same area as the curved profile generated by the spectral line.

For an absorption line, less energy is transported than in the continuum, and this energy is proportional to the area of the line profile. Specifically, the new program performed the following functions:

Reads in an entire spectrum (wavelength, fluxes, errors) from a particular star or target

Reads in a list of wavelengths for which one wants equivalent width and error in equivalent width measurements

For each wavelength:

- determines what order the wavelength is in
- checks the next higher order to see if there is any overlap
- makes a correction to the wavelength order number if there is an overlap
- calculates a pixel range around which it measures the equivalent width
- measures equivalent width
- calculates a pixel range around which it measures the continuum of the spectrum
- measures the continuum
- plots the order with vertical lines marking the central wavelength and the calculated wavelength range over which it measured equivalent width
- plots the order with the continuum fit overlaid
- calculates the error in the measurement of the equivalent width
- saves in a file the wavelength, measured equivalent width, and measured error

The general list of wavelengths to search for in each spectrum is listed in Table 3. However, for each target, these wavelengths had to be corrected for the velocity of the star relative to Earth's rotation (diurnal), the motion of Earth's center about the Earth-Moon barycenter (lunar), the motion of the Earth-Moon barycenter about the center of the Sun (annual), and the motion of the Sun (solar). Thus, to make the wavelengths in the list to match where they *should* be observed in the spectra, the initial radial velocities (found using the SIMBAD online database) had to be corrected for these effects. These velocities were inserted into a new parameter in the header files of our stars (VOBS) and then the IRAF task `rvcorrect` was used to find the corrected radial velocities. Then the corrected wavelength was calculated using

$$\frac{V_{rad}}{c}\lambda_0 + \lambda_0 = \lambda_n \tag{1}$$

where λ_0 is the rest, "zero-velocity" wavelength, and λ_n is the wavelength at which the absorption line should be observed in the spectrum of the star. (This was done for each star, since each has a different radial velocity, position, was observed at a slightly different time, etc.). Though many of the target stars and mini-survey stars do have known radial velocities, a significant portion of our sample did not have radial velocity information available in SIMBAD; we thus had to perform our own radial velocity measurements of these stars using the procedure detailed above. This information will, in theory, help determine upper limits of the equivalent widths at the wavelengths we expect to see absorption in the spectra if there is a gaseous disk. Then we can compare these to the equivalent widths we actually measure and see if the targets have a justified signature of gas.

The second analysis approach, which is what we base our results and discussion on, was a direct, "by-eye" examination, using both IRAF and IDL, of the spectrum of each target along with each comparison star to locate strong absorption lines. From the observed absorption lines in each spectrum, the online Kurucz Atomic Line Database[13] was used to match wavelength values with atomic species based on oscillator strength, cosmic abundance, and correction for the velocity of the star. Prior to this, each line was examined in the raw spectrum of the star to rule out cosmic rays and bad pixels on the CCD, and also compared to the comparison stars and models. From these extensive lists of possible elemental signatures, we have begun to look for similarities and/or differences between one target star and another, between the target stars and their mini-survey companions, and between the previously described spectral models with varying temperatures, gravities, and rotational velocities (depending on the specific target star's characteristics). Additionally, the "by-eye" lists of observed features in each star can eventually be used as new line list inputs for the IDL code mentioned above, providing equivalent width, continuum and error estimates for those wavelengths.

From here, to obtain reliable measure of the temperature of circumstellar gas, the equation

$$\frac{W_\lambda}{\lambda_0} = \frac{\pi \times e^2}{m \times c^2} N \times f \times \lambda_0 \tag{2}$$

can be used, with input parameters including the wavelength observed in the stellar spectrum (λ_0), the measured equivalent width of the absorption line (W_λ), and the oscillator strength (f) of the suspected atomic species. The latter represents the rati of the strength of an atomic transition to the theoretical transition strength of a single electron using a harmonic-oscillator model. Then the relationship between abundance and temperature, for a particular element, can be estimated with[14]

$$\frac{N_k}{N_j} = (weighting\ factor) \times e^{-h\nu_{jk}/kT} \tag{3}$$

where j and k are the levels of ionization and ν_{jk} is the frequency of the photons emitted or absorbed.

One aside possibility that we must consider is that some of the target stars were originally misclassified as shell stars. The Ti II lines 3761.3, 3685.2, and 3759.3 Å were first used by Abt and Moyd (1973) to classify shell stars; the Ca II H and K lines have also been used as indicators. For the portion of the sample currently reduced (eight out of the twelve stars: HD 158352, HD50241, HD77190, HD196724, HD199603,

[13]1995 Atomic Line Data (R.L. Kurucz and B. Bell) Kurucz CD-ROM No. 23. Cambridge, Mass.: Smithsonian Astrophysical Observatory. Online at `http://cfa-www.harvard.edu/amp/ampdata/kurucz23/sekur.html`

[14]from Chapter 2, *Physical Processes in the Interstellar Medium*, Spitzer, 1978

HD223884, HD24863, HD42111, and HD 224463), only the latter four show the standard Ti II line features. However, this is only a preliminary examination and certainly does not rule out the former four as shell stars, especially since these lines have been observed in vary in strength across nights and years. See section 4.3 for detailed discussion of HD 50241, HD 42111, and HD 158352.

4.3. Individual Stars

4.3.1. 50241

HD 50241, or α Pic, was included in the Roberge and Weinberger (2007) sample due to Hempel and Schmitt's 2003 detection and identification of circumstellar gas moving towards the star. Hempel and Schmitt observe a weak Ca II K absorption feature with fairly stable equivalent width that changed radial velocity within six years between observations. They actually suggest the radial velocity change may be due to binarity, noting that HD 50241 is an X-ray source (unexpected for an A-type star), so it is possible that the X-ray emission is originating from an unresolved late-type companion. However, though the Ca II K line is variable, Hempel and Schmitt do not exclusively conclude that the gas must be circumstellar, since the shape of the line does not change (as it does in other objects in their sample, which they take as a stronger sign of circumstellar versus interstellar origin). In accordance with Cheng et al. (1992)'s negative dust detection (using IRAS bandpasses 12, 25, and 60 μm), Roberge and Weinberger did not detect any IR excess at 24 or 70 μm around HD 50241.

From our spectra, we see no evidence of strong Ca II, Na I, or Ti II absorption in HD 50241, contrary Hempel and Schmitt's data. There is a possible detection of Ca II 3933 Å, but its equivalent width is roughly an order of magnitude less than that detected in HD 158352 (discussed below). Also, it is difficult from our data to constrain what is circumstellar versus interstellar because we do not currently have adequate spectra of nearby comparison stars. However, based on several nights of observation, the HD 50241 appears to show Cr I, Ti I, Mn I, and Fe I.

Using the procedure outlined in section 4.1, the radial velocity of HD 50241 was found to vary substantially from both the referenced value (20.6 kms^{-1}, Wilson 1953) and from night to night. This variation was found by chance when attempting to obtain a reliable correction factor for detecting absorption lines in our spectra. To examine the system in more detail, we obtained further observations in March 2008, producing the following table and plot of radial velocity versus the day of year of the observation (Figure 6). The different colors correspond to the three different models used in correlation with the system. HD 50241 is a type A7, giving $\sim T_{eff}$ of 7500 K, and has vsini 206 kms^{-1} (Royer, Zorec, & Gomez 2007). (Note: Many other models were attempted with HD 50241 before obtaining relatively steady radial velocity values; their `xcsao` output is not given here. This object was our first attempt at determining the "true" radial velocity.)

To explain this anomalous radial velocity variability in HD 50241, we suggest that it exists as a spectroscopic binary (single-line). This situation arises when the primary star is under some gravitational influence of a (less luminous) companion (whose spectrum is hidden by the much greater flux of the primary star). The observed radial velocity variation is observable in the Doppler shift of the primary star's spectral lines as it moves towards (blue shifted) and away (red shifted) from the observer (around the shared center of mass with its companion). A recent agreement with this explanation is the paper by Golden and Makarov (2006), in which they outline the development and use of an automated algorithm to obtain orbital fits of stars with stochastic solutions from the Hipparcos catalog. They suggest that these stars are prime suspects for unresolved/unknown binaries. At a confidence level of 99%, they produce orbital fits for 65 stars and claim to discover 54 previously unknown binary systems, including HD 50241.

Fig. 6.— Varying radial velocities of HD 50241 as calculated by fitting a template with effective temperature 7500 K, log(g) of 3.5, and vsini of (red) 200 kms^{-1}, (blue) 100 kms^{-1}, and (black) 10 kms^{-1}. The rotational velocity of 50241 as calculated by Royer et al. (2007) is 206 kms^{-1}.

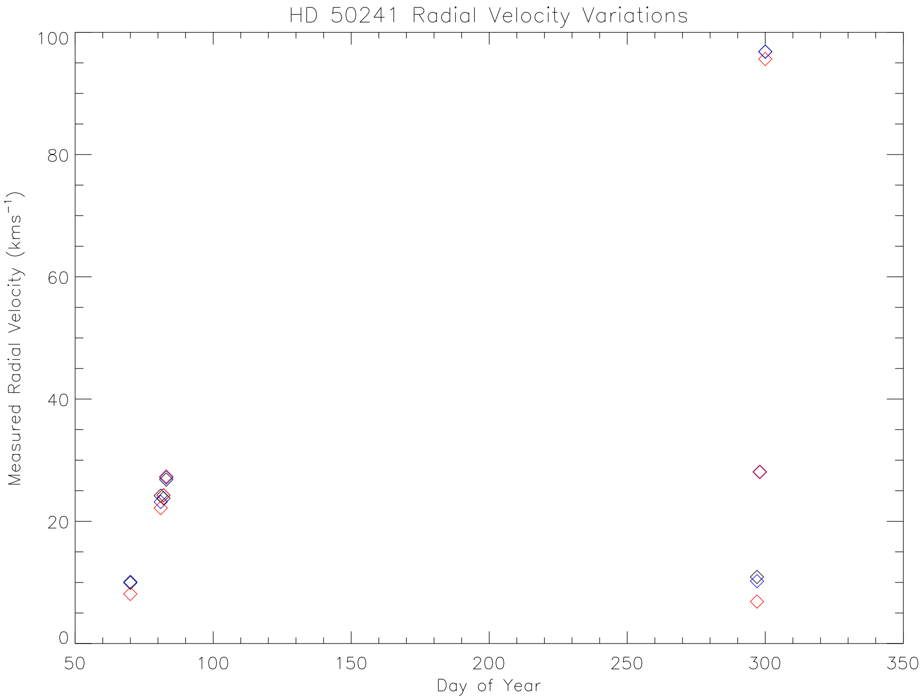

4.3.2. 42111

F. G. W. Struve (1831) first noted this triple system: component A (HD 42111) is a 6.0 mag A3Vn (Hauck and Jaschek 2000) star with component B (HD 42092), which is a 7.0 mag A0 star (although this classification is suspect since it is based on older observations) at a separation distance 29.3 arsec and orienation 114 deg. Component C is an 8.9 mag ∼G0 type star (based on colors B-V and V-K) and is 118.1 arcsec and 106 deg away from component B. (These data were obtained from the Catalog of Components of Double & Multiple stars (Dommanget & Nys 2002) unless otherwise noted.) Plates from Feburary 1958 showed a shell spectrum, but by 1959 these characteristics had weakened significantly, though the Fe II lines were still sharp and prominent (Slettebak 1963). Cowley and Hiltner (1968) reported no shell lines seen between 1966 and 1968, but by 1982 Slettebak's observations showed the spectrum broadened by rotation, with the exception of strong and sharp Ca II H and K lines, and the sharp Fe II 4233, 4549, and 4584 Å lines, again apparently due to the circumstellar shell. These observations were confirmed by Jaschek et al. (1988), with additional Ti II 3759 and 3761 Å lines seen, although weaker than previous observations in 1983 and 1984 (yet stronger than in 1980, when Slettebak observed no Ti II lines, as cited in his 1982 paper). The 1983 observations also showed weak Fe II at 4233 and 4549 Å. Grady et al. (1996) added *International Ultraviolet Explorer* data to the sample, and (though not the first to do so) pointed out changes in the shell line visibility on timescales of years; they connected this variability with that of the accreting gas toward

β Pic and the long-term variability of Herbig Ae stars. However, Abt et al. (1997) note that Ti I has an ionization potential of 6.81 eV, while the three Ti II lines have potentials of 0.6 eV, combining to an excitation of 7.4 eV, which requires higher temperatures that the dust disks seen around β Pic. (From their sample Abt also constrains the radii of the disks to about seven stellar radii, much closer to the star than β Pic's $\sim$ 50,000 stellar radii disk.) Interestingly, in our spectra of HD 42111 we observe the characteristic Fe II shell lines, as well as the bluer Ti II lines (3759, 3761, possibly 3685 Å), but not the Ca II H and K features, which were supposedly the most recognizable/easily detectable in previous shell star samples. Overall, other prominent species appear to be Fe I, Ti I, and possibly Mn I. Using the procedure outlined in section 4.1, the radial velocity of HD 42111 was found to vary from the referenced value of 34.2 kms^{-1} (Wilson 1953). In Table 4.3.2 is the output of `xcsao`: As can be seen, the radial velocity ranged from 17-23 kms^{-1} on October 24, 2007, to 28-32 kms^{-1} on the 25th, to 116-118 kms^{-1} on the 27th. (It is spectral type A3, giving T$_{eff}$ of $\sim$8500 K, and has a referenced vsini of 242 kms^{-1} (Royer, Zorec, & Gomez 2007).) The large variation in radial velocity instead suggests a new, (non-visual) spectroscopic companion (see Section 5).

4.3.3. 158352

Abt and Moyd's 1973 study of 66 metallic-line and 123 normal A5-A9 IV or V type stars produced just eight shell star candidates, and HD 158352 was one of these, displaying weak Ti II features at 3759 and 3761 Å. Dominy and Smith (1977) confirmed this detection, as did Slettebak in 1980, although the latter noted weaker shell features than many of the other Abt-Moyd objects (Slettebak 1982). Andrillat et al. (1983) noted that while they detected two absorption components of Ca II K in 1981, these structures had vanished by 1983. Yet Hobbs (1986) found a Ca II K abundance of 2.2×10^{11} cm (equivalent width 19 mÅ) in HD 158352 (though no Na I), and Jaschek, Jaschek and Andrillat (1988) reported their 1981 and 1984 observations showed Ca II K and H absorption. Lagrange-Henri et al. (1990) reported a Ca II K equivalent width of 28 ± 5 mÅ, and a Na I equivalent width of 18 ± 5 mÅ. Using 1994 *International Ultraviolet Explorer* observations, Grady et al. (1996) reported detection in HD 158352 of transitions to the 0 eV level of the Fe II ground configuration (which are also produced in the diffuse interstellar medium) and not to the J-levels or higher metastable levels, which indicates circumstellar origin; they thus reported no detectable circumstellar gas. Follow-up observation in 1996 by Jaschek and Andrillat (cited in 1998) found no indication of a shell in the Paschen region (λ8100–8900 Å) but did see a strengthening of Ca II since 1989.

The fact that they did not see Ti II in HD 158352 led Abt, Tan & Zhou (1997) to suggest it does not harbor a hot inner disk of gas; their "working hypothesis" is that all A-type stars rotating near their limits (around 200 kms^{-1}) have shells, but only for one-quarter of the time. Rhee et al. (2007) cross correlated Hipparcos stars with the IRAS catalogs to find stars with excess 60 μm emission and reported HD 158352 as having a dusty debris disk at 85 AU, with the dust temperature of 70 K and dust mass of $5.39 \times 10^{-2}\ M_{\oplus}$, producing a fractional IR luminosity (L_{IR}/L_*) value of 6.81×10^{-5}. Roberge and Weinberger fit their own observations with a 76.1 K dust ring at 62 AU (assuming blackbody dust grains; 191 AU if assuming silicates) with $L_{IR}/L_* =\ 9.29 \times 10^{-5}$. Most recently, Eisner et al. (2004) found no excess 2.2 μm emission with the near-IR Palomar Testbed Interferometer. Other recent observations (Grady et al. 1996, Eritsyan et al. 2002) suggest it is likely an evolved shell star or Vega-like object.

To characterize the disk of HD 158352, our goal was to obtain a reliable measure of temperature of circumstellar gas, as well as the velocity of the gas in relation to the star. These parameters can help constrain the location of the gas around the star and in relation to any dust, saying something about dust-grain interaction, the stage of evolution of the system and perhaps information about planetesimal growth and movement. As with our other objects, the first step in analyzing the spectra of HD 158352 was to find the correct radial velocity, then use it to shift the observed absorption lines to their "zero-velocity" rest position in order to identify the atomic species associated with each line. Though the radial velocity of HD 158352 is referenced in SIMBAD as -36.1 kms^{-1} (Wilson 1953), we used our procedure outlined in section 4.1 to check this value and obtained the results in Table 4.3.3.

Thus we found good agreement with the literature values of the radial velocity, based on this model fitting (spectral type A8, so T$_{eff}$ ∼7500 K, and vsini referenced as 180 kms^{-1}). However, applying this correction did *not* produce a match in our spectra to the actual observed wavelengths of known "standards", such as Ca II H and K lines, and the Na I doublet. By working backwards with the known, zero-velocity wavelength values of these standard lines and the wavelength values observed in our spectra, we obtained a radial velocity estimate of approximately -53 kms^{-1} and used this value for wavelength corrections and further analysis. In relation to the referenced radial velocity of -36.1 kms^{-1} (Wilson 1953), the gas appears blue shifted by 17 kms^{-1} relative to the star.

Using comparison star HD 158737, we examined the spectra of HD 158352 and recorded observed absorption lines that did not appear to correlate with bad pixels and cosmic rays in the raw, 2-D spectra and that did not appear in the comparison. This process actually produced very few reliable detections, even after applying our radial velocity correction. Some candidate absorption lines had equivalent widths that were low enough to make their detection questionable (so, the line is likely just noise), or did not have realistic corresponding atomic species (according to the Kurucz database). However, overall HD 158352 most likely shows Ti I, Co I, some Ni I and Fe I, and perhaps Cr I.

The lines that were definitely strongly detected were the Ca II H and K lines, as well as the Na I doublet lines. We chose to initiate further analysis on these. After continuum normalizing each night, and the observations of comparison stars HD 158737 and HD 157089, we examined HD 158352 across the three nights of March, 2008 observation, and against the comparison stars (observed on 21 March). The IRAF task `bcvcorr` was also used to determine the "correct" position of each species based on the barycentric velocity and heliocentric velocity corrections for the specific night; that is, where the line should be expected in our spectra. (This correction proved to alter the wavelength values by at most a few hundredths of an angstrom; they are shown on the comparison spectra below.)

From Figure 9, we conclude that the Ca II 3932 Å absorption is most likely interstellar and not circumstellar due to its obvious presence in both comparison stars. The Ca II lines at 3968 Å is not as evidently interstellar—in HD 157089, the line center is right on the edge of absorption feature, which itself is split (whereas it does not appear to be as prominently in HD 158352, although we discuss this in Section 5). In HD 158737, the line center falls on the edge of a weak feature. After renormalizing the continuum in HD 158737 around this weak feature, we calculated the equivalent widths in it and HD 158352 to obtain the following results:

This indicates that perhaps the feature in HD 158737 does, indeed, *not* correspond to the observed Ca II in HD 158352. However, this might imply the Ca II H line was interstellar while the K line was circumstellar, which we find highly unlikely. Instead, it is more probable that the H line is interstellar but just too weak in HD 158737 and HD 157089 to be detected. The oscillator strength of the K line is almost twice that of the H line (log(gf) 0.134 for K, -0.166 for H)[15], and the log(N$_a$) of Ca II K in HD 158352 is $\sim 11.35 \pm 0.015$,

[15]Kurucz Atomic Line Database

Fig. 7.— Ca II 3932 Å detection across nights 21-23 March 2008. Created by Aki Roberge.

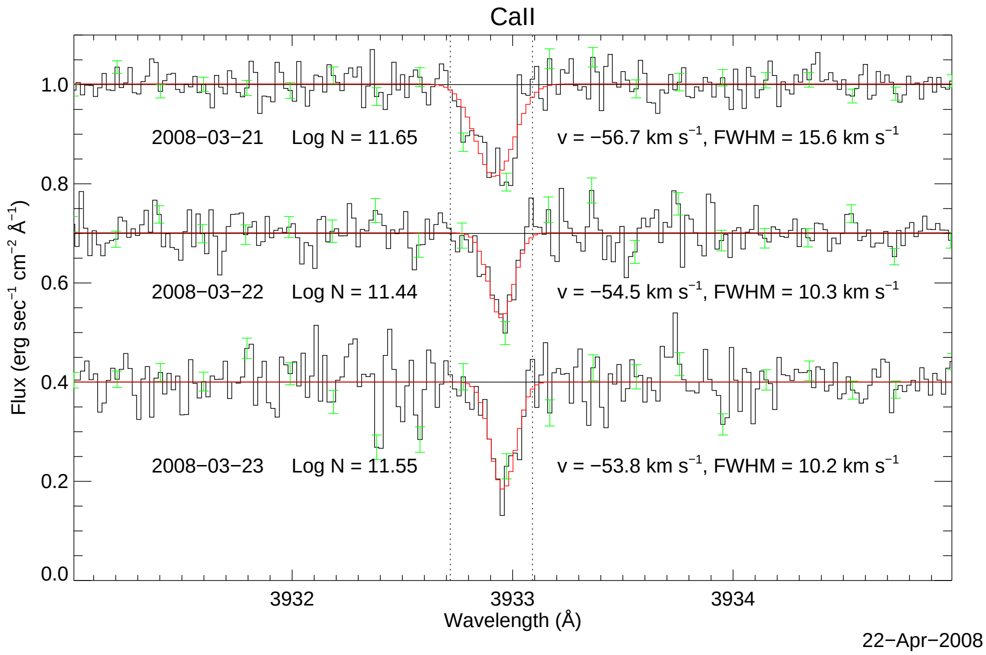

Fig. 8.— Ca II 3968 Å detection across nights 21-23 March 2008. Created by Aki Roberge.

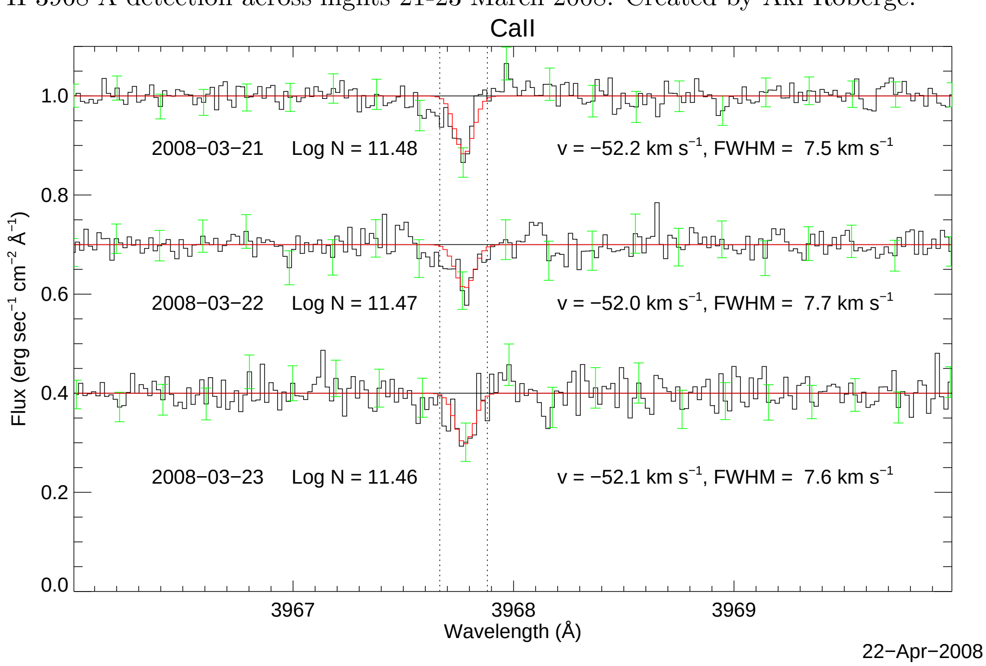

whereas it is $\sim 10.91 \pm 0.035$ for HD 158737 and $\sim 10.39 \pm 0.0027$ for HD 157089. So, it seems the strength of the Ca II feature is stronger overall in HD 158352; this probably explains the the weak/non-detection of the H line in the companion stars.

Fig. 9.— Ca II 3932 Å detection, compared with detection in comparison stars HD 15789 and HD 158737, on 21 March 2008.

Fig. 10.— Ca II 3968 Å detection, compared with detection in comparison stars HD 157089 and HD 158737, on 21 March 2008.

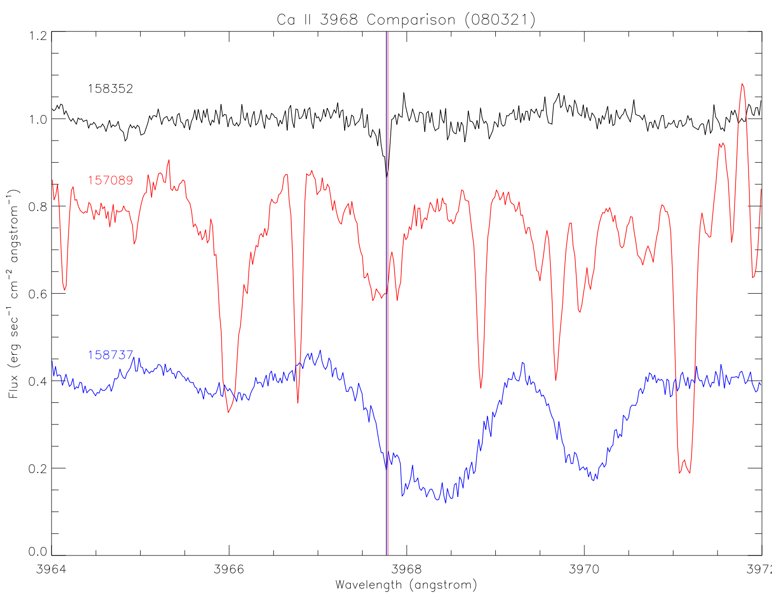

Figure 12 seems to indicate circumstellar origin for the Na I observed in HD 158352. There is no real overlap between the target and comparison absorption features (we believe the close-by line in HD 157089 is another species from the stellar photosphere). We determined the measurements (Table 4.3.3 for these Na I lines using equation 2 in Section 4.2. The wavelength ranges over which the equivalent width was measured were kept constant.

Fig. 11.— Na I 5888 Å detection across nights 21-23 March, 2008. Created by Aki Roberge.

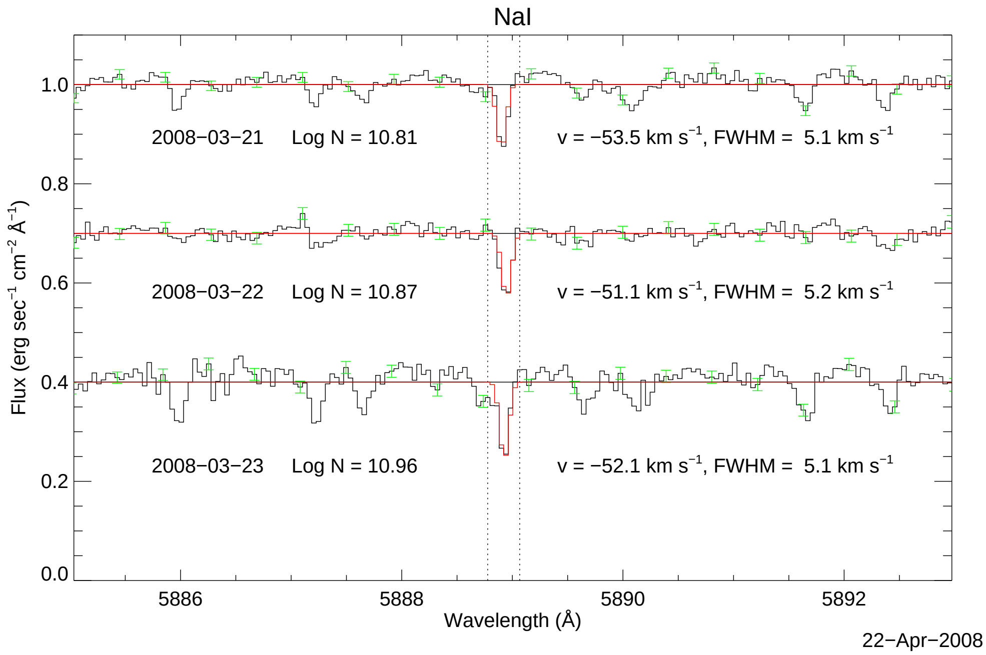

Fig. 12.— Na I detection (both wavelengths), compared with detection comparison stars HD 157089 and HD 158737, on 21 March 2008

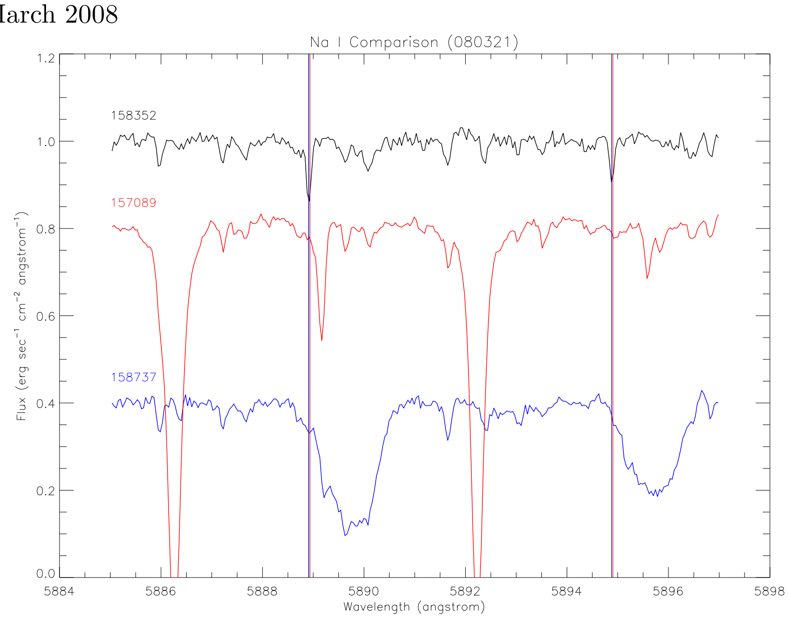

The calculated abundance values are not as conclusive as the plot, especially for HD 158737, which seems to show equal or greater abundance than HD 158352 in (at least) the Na I 5888 Å line. However, these results are preliminary and dependent upon a prior continuum fit and normalization of the spectra individually, which could introduce extra measured flux.

5. Discussion

From a review of existing literature and our radial velocity calculations, both HD 50241 and HD 42111 were found to be (highly likely) spectroscopic binaries. This accounts for their differing radial velocity measurements. We believe HD 50241, at least, may be categorized as a single-line spectroscopic binary, with a smaller and less luminous companion, perhaps an M dwarf type star, that is causing slight gravitational shift in the wavelengths over the course of our observations. From our observations and measurements of varying radial velocity in HD 50241, the orbit appears highly irregular and eccentric, since the data show no obvious periodicity (see Figure 6). Our limited observations of HD 42111 do not allow for a similar conclusion about the radial velocity. However, the variation is most likely *not* due to either companion of HD 42111. A rough calculation using

$$a = \frac{G(M+m)}{v^2} \tag{4}$$

where a is the center of mass of the rotating system (taken to be half of the separation distance, $\sim$5500 AU) and assuming the masses of HD 42111A and 42111B to be $\sim$2.9 $M_\odot$ yields an expected velocity varation of 1.39 kms^{-1} due to component B. (Component C is even farther away and fainter, so would have an even smaller affect on the observed velocity of component A.) We observe, as in Table 4.3.2, a much greater variation in radial velocity, and over only three nights. This makes a strong case for HD 42111 being a spectroscopic binary; more observations over greater timescales would help confirm or dispell this theory.

If we measure other targets in our sample to have variable radial velocities, indicating they are spectroscopic binaries, a careful examination of all shell stars might reveal varying radial velocity as a significant trend and aid in classifying and explaining shell characteristics. One possibility is that the lines that we are observing in our shell stars may not be coming from a circumstellar disk per se, but instead could be due to interaction with an M dwarf wind/outflow. This hypothesis can be examined by further comparison of the lines seen around HD 50241 and HD 42111 with each other, with those expected in the wind of an M dwarf star, with those found around other target stars, and with those found around HD 158352, a known debris disk system. It may be that all or many stars previously classified as A shell stars that do not show significant IR excess are actually binaries, and perhaps are accreting material from their companions.

Another interesting aspect of HD 50241 is the variability of the shell lines, noted in section 4.3.1. While they do not include this object in their study of the variability of hot inner disks, Abt et al. (1997) pose the question of whether disk appearance and disappearance could be caused by precessing rotational axes—this could only occur if the star has a companion orbiting outside the rotational plane. If the orbital period of the binary is less than 100 days, the secondary might be able to cause sufficient precession of the primary's rotational axis to make the disk alternately visible, and then not visible, in front of the stellar photosphere on the timescales we observe.

While the detection of Ca II 3932 Å in two comparison stars of HD 158352 generally rules out circumstellar origin for this gas, one caveat is the appearance in the 21 March observation of possible doubling of this Ca line. There is a component that does not correspond to the line center but is still well defined. If we believe that this component is significantly (outside the error bars) below the continuum, it may be caused by some variability in the actual composition of the disk—calcium gas evaporation in the disk could occur across the time of our observations, causing the component, having a different velocity around the star, to disappear during subsequent nights. As Lagrange et al. (1987) and Beust et al. (1990, and subsequent papers in the series) suggest, transient spectroscopic events observed in β Pic, albeit at much shorter timescales, are evidence for cometary material subliminating or evaporating as it passes close to the star, analogous to Sun-grazing comets in our Solar System. More observations of HD 158352 over different time scales and at higher signal to noise are necessary to validate this Ca variability hypothesis (by observing more evaporation occurrences in calcium and/or other detected species) in HD 158352.

The positive identification of circumstellar Na I in HD 158352 is exciting but perhaps not surprising, as atomic sodium was also strongly detected in β Pic and the transition itself (Einstein coefficient) is very strong. Interestingly, the IR excess ($L_{IR}/L_* = 9.29 \pm 0.26 \times 10^{-5}$) found by Roberge and Weinberger around this object is anomalously high for its estimated age (750 ± 150 Myr, Móor et al. 2006). This could indicate a larger amount of dust relative to gas as compared to β Pic if this object has a different production mechanism for the dust and gas. Additionally, the relative radiation pressure of HD 158352 is greater than that of β Pic. This is estimated with the ratio δ of radiation to gravitational forces acting on a grain (dust particle) surrounding a star (assuming spherical, black-body grains with radius a):

$$\delta \equiv \frac{F_{rad}}{F_{grav}} = \frac{0.57}{a_{\mu m}\rho}\frac{L_*}{L_\odot}\frac{M_\odot}{M_*} \tag{5}$$

Given the same grains, β Pic's relative radiation pressure is roughly half that of HD 158352. Chen et al. (2007) provide in great detail a model for the origin of β Pic's detected sodium (although the detection was via scattered emission, Brandeker et al. 2004). Possible origins they suggest include infalling refractory bodies, collisions between dust grains, and photon-stimulated desorption (PSD) from surfaces resembling SiO_2. Backman and Paresce (1993) point out that the "cometary hypothesis is not as far-fetched as it might seem, since small Sun-grazing comets that are totally disrupted in the ensuing collision are known to occur in our own Solar System as often as 10 times per year (Michels et al. 1982)." Beust and Valiron (2007), in their analysis of the gas in β Pic, favor this *Falling Evaporating Bodies* (FEB) hypothesis, but partially because it explains the lack of Na I emission at high latitutdes in the disk (since the Na I ionized would be quickly photoionized and no longer experience radiation pressure). The high IR flux of HD 158352, if taken to represent a larger dust mass, may be indicative of grain-grain collisions in the disk producing enhanced sodium, especially if radiation is driving grains to smash into each other. We also observe the gas to be blueshifted (as noted in 4.3.3), i.e. outflowing (whereas the controversy surrounding β Pic is the stability of its gas, e.g. Lagrange et al. 1998, Brandeker et al. 2004), which is supported by the higher relative radiation pressure. Further analysis of our observations can hopefully produce temperature and velocity estimates for the gas, which will greatly influence the above discussion and the location of the gas in the disk (and in relation to the dust). For example, if the gas and dust are correlated in location, this would point towards grain-grain collision as the gas creation mechanism, since such a process would mix the dust and gas simultaneously (i.e., Fernández, Brandeker & Wu 2006).

6. Conclusions

This paper has sought to examine a peculiar population of A-shell stars that show evidence for close-in, rotating material in order to better understand the relationship between the circumstellar gas and dust. Using optical spectra, we searched for strong, narrow absorption lines and identified the most likely atomic species responsible for the lines. Specifically, we identified Ca II as interstellar and Na I as circumstellar in object HD 158352, a probable debris disk candidate. Additionally, we observed significant radial velocity variability in the spectra of HD 50241 and HD 42111 and suggest that these objects have spectroscopic binary companions that have previously gone undetected (although theorized in the case of HD 50241). Further analysis will include complete reduction of all current observations, temperature and distance calculations for the gas, checking all of the target stars for radial velocity variation, completing observation of all targets in our sample, and continuing to observe the spectroscopic-binary candidates to determine their periods. Also, additional observations of HD 158352 will help determine if the observed sodium could be variable, indicating another candidate system for the FEB theory.

7. Acknowledgments

This work is supported by the Carnegie Institution of Washington NASA Astrobiology Institute. This research has also made significant use of the SIMBAD database, operated at CDS, Strasbourg, France and NASA's Astrophysics Data System.

J.K.T. would like to thank Dr. I-lok Chang for informing her of the DTM, Dr. Nathan Harshman for his continuous support and enthusiasm, Dr. Alceste Bonanos and Dr. Mercedes Lopez-Morales for their help in radial velocity determinations, and Dr. Alycia Weinberger for her patience, ingenuity, and taking a chance.

REFERENCES

Abt, H. A. 2008, 17, 499

Abt, H. A., Tan, H., & Zhou, H. 1997, ApJ, 487, 365.

Abt, H. A. & Moyd, K I. 1973, ApJ, 182, 809

Anderson, J. & Nordstróm, B. 1977, Astr. Ap. Supp., 29, 309

Andrillat, Y., Jaschek, M., & Jaschek, C. 1983, Hvar Obs Bull. 7, 193

Aumann, H. H. 1985, PASP, 97, 885

Backman, D. E., & Paresce, F. 1993, Protostars and Planets III, 1253

Bastien, P. 1982, A&AS, 48, 153

Bernstein, R. A., Schectman, S. A., Gunnels, S. M., Mochnacki, S., & Athey, A. E. 2003, SPIE, 4841, 1694

Beust, H. & Valiron, P. 2007, A&A, 466, 201

Beust, H., Vidal-Madjar, A., Ferlet, R., Lagrange-Henri, A. M. 1990, A&A, 236, 202

Brandeker, A., Liseau, R., Olofsson, G., Findlund, M. 2004, A&A, 413, 681

Breger, J. 1962, Ann. Astrophys., 25, 1

Breger, M. 1978, ApJ, 223, 180

Cheng, K. P., & Neff, J. E. 2003, AJ, 125, 868

Chen, C. H. et al., 2007, ApJ, 666, 466

Chen, C. H., & Jura, M. 2003, ApJ, 582, 443

Churchill, C. W. 1995, University of California Lick Observatory Technical Report No. 74

Cowley, A. P. & Hiltner, W.A. 1968, PASP, 80, 685

Czechowski, A., & Mann, I. 2007, ApJ, 660, 1541

Dent, W. R. F., Greaves, J. S., & Coulson, I. M. 2005, MNRAS, 359, 663

Dommanget, J. & Nys, O. 2002, CCDM, Observations et Travaux 54, 5.

Eisner, J. A., Lane, B. F., Hillenbrand, L. A., Akeson, R. L., & Sargent, A. I. 2004, ApJ, 613, 1049

Evans, D. S. 1967, IAU Symp. 30, 57

Fernández, R., Brandeker, A., & Wu, Y. 2006, ApJ, 643, 509

Garcia Lopez, R., Natta, A., Testi, L., & Habart, E. 2006, A&A, 459, 837

Gautier, T. N., et al. 2007, ApJ, 667, 527

Goldin, A., & Makarov, V. V. 2006, ApJS, 166, 341

Grady, C. A., Perez, M. R., Talavera, A., McCollum, B., Rawley, L. A., England, M. N., & Schlegel, M. 1996, ApJ, 471, L49

Greenstein, J. L. 1953, ApJ, 117, 269

Greves, J. 2005, Science, 307, 68

Habing H., Dominik, C., Jourdain de Muizon, M., Laureijs, R., Kessler, M., et al. 2001, Astron. Astrophys., 365, 545-561

Hauck, B. & Jaschek, C. 2000, A&A, 354, 157

Hempel, M., & Schmitt, J. H. M. M. 2003, A&A, 408, 971

Hildebrand, R. H. 1983, QJRAS, 24, 267

Hobbs, L. M. 1986, ApJ, 308, 854

Holweger, H., Hempel, M., & Kamp, I. 1999, A&A, 350, 603

Kelson, D. D., Illingworth, G.D., van Dokkum, P.G., & Franx, M. 2000, ApJ, 531, 159

Kelson, D. D. 2003, PASP, 115, 688

Kelson, D. D., Illingworth, G.D., Franx, M., & van Dokkum, P.G. 2006, ApJ, 653, 159

Kurucz, R. L. & Bell, B. 1995, Atomic Line Data, Kurucz CD-ROM No. 23. Cambridge, Mass.: Smithsonian Astrophysical Observatory

Kwok, S. 1980, ApJ, 236, 592

Jaschek, M., Jaschek, C., & Andrillat, Y. 1988, A&AS, 72, 50

Jaschek, C. & Andrillat, Y. 1998, A&AS, 130, 507

Jayawardhana, R., Hartmann, L., Fazio, G., Scott, F. R., Telesco, C. M., & Pia, R.K. 1999, Ap., 521, L129

Lagrange, A. M., Ferlet, R., & Vidal-Madjar, A. 1987, AAp, 173, 289

Lagrange, A. M., et al. 1998, A&A, 330, 1091

Lagrange-Henri, A. M., Ferlet, R., Vidal-Madjar, A., Beust, H., Gry, C., & Lallement, R. 1990. AApS, 85, 1089 Lallement, R., Welsh, B. Y., Vergely, J. L., Crifo, F., & Sfeir, D. 2003, A&A, 411, 447

Lecavelier des Etangs, A., Vidal-Madjar, A., & Ferlet, R. 1996, A&A, 307, 542

Lecavelier des Etangs, A., et al. 1997, A&A, 325, 228

McCabe, C., Ghez, A. M., Prato, L., Duchêne, G., Fisher, R. S., & Telesco, C. 2006, ApJ, 636, 932

Meyer, M., et al. 2008, ApJ, 673, L181

Michels, D. J., Sheeley, N. R., Howard, R. A., & Koomen, M. J. 1982, Science, 215, 1097

Móor, A., Ábrahám, P., Derekas, A., Kiss, C., Kiss, L. L., Apai, D., Grady, C., & Henning, T. 2006, ApJ, 644, 525

Morgan, W. W. 1932, ApJ, 76, 144

Natta, A., Testi, L., Calvet, N., Henning, T., Waters, R.,& Wilner, D. 2007, Protostars and Planets V, 767

Pascucci, I., et al. 2006, ApJ, 651, 1177

Reddish, V. C. 1967, Publ. of the Royal Obs., Edinburgh, v. 6, no. 2

Redfield, S. 2007, ApJ, 656, L97

Redfield, S., Kessler-Silacci, J. E., & Cieza, L. A. 2007, ApJ, 661, 944

Reid, M. J., Muhleman, D. O., Moran, J. M., Johnston, K. J., Schwartz, P. R. 1977, ApJ, 214, 60

Rhee, J. H., Song, I., Zuckerman, B., & McElwain, M. 2007, ApJ, 660, 1556

Rieke, G. H., et al. 2005, ApJ, 620, 1010

Roberge, A., Feldman, P. D., Lecavelier des Etangs, A., Vidal-Madjar, A., Deleuil, M., Bouret, J.C., Ferlet, R., & Moos, H. W. 2002, ApJ, 568, 343

Roberge, A. & Weinberger, A. J. 2008, ApJ, 676, 509

Royer, F., Zorec, J. & Gomez, A. E. 2007, A&A, 463, 671

Silverstone, M. D. et al. 2006, ApJ, 639, 1138

Skrutskie, M. F., Dutkevitch, D., Strom, S. E., Edwards, S., Strom, K. M., & Shure, M. A. 1990, AJ, 99, 1187

Sletteback, A. 1963, ApJ, 138, 118

Sletteback, A. 1975, ApJ, 197, 137

Slettebak, A. 1982, ApJS, 50, 55

Smith, B. A., Terrile, R. J. 1984, Science, 226, 1421

Spangler, C., Sargent, A. I., Silverstone, M. D., Becklin, E. E., & Zuckerman, B. 2001, ApJ, 555, 932

Strom, S. E., Strom, K. M., Yost, J., Carrasco, L., Grasdalen, G. 1972, ApJ 172, 353

Struve, O. 1932, ApJ, 76, 85

Takeuchi, T., & Artymowicz, P. 2001, ApJ, 557, 990

Telesco, C. M., 2000, ASP Conf., Vol 219

Tull, R. G., MacQueen, P. J., Sneden, C., & Lambert, D. L. 1995, PASP, 107, 251

Weinberger, A. et al. 2002, ApJ, 566, 409

Williams, T. & Ledlow, M. 1998, Iraf Reduction of Capilla CCD Images,

`http://www.phys.unm.edu/ cpo/html/twhtml/iraf/iraftut.html`

Wilson, R. E. 1953, Carnegie Inst. Washington D.C. Publ. 601, 1953

Zuckerman, B., Forveille, T., & Kastner, J. H. 1995, Nature, 373, 494

Zuckerman, B. 2001, ARAA, 39, 549

This preprint was prepared with the AAS LaTeX macros v5.0.

Table 3: General list of wavelengths indicative of circumstellar gas.

Blue MIKE Band 3350–5000 Å)	Atomic Species
3369.563	Ni I
3391.039	Ni I
3392.983	Ni I
3440.606	Fe I
3578.684	Cr I
3593.481	Cr I
3605.321	Cr I
3719.935	Fe I
3737.131	Fe I
3859.911	Fe I
3933.663	Ca II
3944.006	Al I
3961.52	Al I
3968.469	Ca II
4030.753	Mn I
4033.062	Mn I
4034.483	Mn I
4226.728	Ca I
Red MIKE Band (4900–9500 Å)	
5889.951	Na I
5895.924	Na I
6707.749	Li I
6707.749	Li I
6707.749	Li I
6707.773	Li I
6707.773	Li I
6707.773	Li I
6707.899	Li I
6707.9	Li I
6707.918	Li I
6707.918	Li I
6707.923	Li I
6707.924	Li I
6707.924	Li I
6707.924	Li I
6707.925	Li I
6708.069	Li I
6708.07	Li I
6708.074	Li I
6708.075	Li I
7664.911	K I
7698.974	K I

Table 4. Radial Velocity Determination, HD 50241

Date	Model[1]	Peak Height	Radial Velocity (kms^{-1})
March 11, 2007	teff_7500_g3.5_v200	0.817	8.118
	teff_7500_g3.5_v100	0.813	10.094
	teff_7500_g3.5_v10	0.599	9.946
October 24, 2007	teff_7500_g3.5_v200	0.778	6.871
	teff_7500_g3.5_v100	0.773	10.205
	teff_7500_g3.5_v10	0.572	10.895
October 25, 2007	teff_7500_g3.5_v200	0.836	28.074
	teff_7500_g3.5_v100	0.829	28.121
	teff_7500_g3.5_v10	0.611	28.052
October 27, 2007	teff_7500_g3.5_v200	0.803	95.626
	teff_7500_g3.5_v100	0.798	96.823
	teff_7500_g3.5_v10	0.589	96.850
March 21, 2008	teff_7500_g3.5_v200	0.830	22.174
	teff_7500_g3.5_v100	0.824	23.173
	teff_7500_g3.5_v10	0.608	24.196
March 22, 2008	teff_7500_g3.5_v200	0.807	24.250
	teff_7500_g3.5_v100	0.802	24.279
	teff_7500_g3.5_v10	0.590	23.783
March 23, 2008	teff_7500_g3.5_v200	0.828	27.336
	teff_7500_g3.5_v100	0.822	27.159
	teff_7500_g3.5_v10	0.606	26.820

[1]The model names are constructed as follows: 't09000' or 'teff9000' = T_{eff} of 9000 K, 'g40' or '_g4.0' = log(g) of 4.0, 'v2r10' or 'v10' = 10 kms^{-1} project rotational velocity

Table 5. Radial Velocity Determination, HD 42111

Date	Model[1]	Peak Height	Radial Velocity (kms^{-1})
October 24, 2007	t08500g30v2r230.fits	0.837	18.768
	t08500g30v2r240.fits	0.836	18.548
	t08500g30v2r250.fits	0.835	18.212
	t08500g30v2r260.fits	0.833	18.161
	t08500g35v2r230.fits	0.787	18.979
	t08500g35v2r240.fits	0.786	18.726
	t08500g35v2r250.fits	0.785	18.611
	t08500g35v2r260.fits	0.784	18.647
	t08500g40v2r230.fits	0.752	19.239
	t08500g40v2r240.fits	0.754	19.706
	t08500g40v2r250.fits	0.753	19.640
	t08500g45v2r230.fits	0.743	20.125
	t08500g45v2r240.fits	0.742	20.029
	t08500g45v2r250.fits	0.741	19.921
	t08500g50v2r230.fits	0.749	20.736
	t08500g50v2r240.fits	0.748	20.621
	t08500g50v2r250.fits	0.747	20.695
October 25, 2007	t08500g30v2r230.fits	0.812	28.865
	t08500g30v2r240.fits	0.810	28.807
	t08500g30v2r250.fits	0.809	28.809
	t08500g35v2r230.fits	0.762	29.873
	t08500g35v2r240.fits	0.761	30.174
	t08500g35v2r250.fits	0.760	30.025
	t08500g40v2r230.fits	0.727	31.001
	t08500g40v2r240.fits	0.729	31.296
	t08500g40v2r250.fits	0.728	31.390
	t08500g45v2r230.fits	0.718	31.569
	t08500g45v2r240.fits	0.717	31.632
	t08500g45v2r250.fits	0.716	31.696
	t08500g50v2r230.fits	0.725	31.773
	t08500g50v2r240.fits	0.723	31.809
	t08500g50v2r250.fits	0.722	31.848
October 27, 2007	t08500g30v2r230.fits	0.844	117.211
	t08500g30v2r240.fits	0.843	117.007
	t08500g30v2r250.fits	0.842	117.217
	t08500g35v2r230.fits	0.794	117.845
	t08500g35v2r240.fits	0.794	117.966
	t08500g35v2r250.fits	0.793	118.027
	t08500g40v2r230.fits	0.758	118.043
	t08500g40v2r240.fits	0.760	118.324
	t08500g40v2r250.fits	0.759	118.633
	t08500g45v2r230.fits	0.748	118.259
	t08500g45v2r240.fits	0.747	118.332
	t08500g45v2r250.fits	0.747	118.605
	t08500g50v2r230.fits	0.754	118.430
	t08500g50v2r240.fits	0.753	118.677
	t08500g50v2r250.fits	0.752	118.515

[1]The model names are constructed as follows: ‘t09000’ or ‘teff9000’ = T_{eff} of 9000 K, ‘g40’ or ’_g4.0’ = log(g) of 4.0, ‘v2r10’ or ‘v10’ = 10 kms^{-1} project rotational velocity

Table 6. Radial Velocity Determination, HD 158352

Date	Model[1]	Peak Height	Radial Velocity (kms^{-1})
March 21, 2008	teff7500_g3.5_v10.fits	0.603	-38.040
	teff7500_g3.5_v100.fits	0.807	-39.531
	teff7500_g3.5_v200.fits	0.795	-42.942
March 22, 2008	teff7500_g3.5_v10.fits	0.603	-36.730
	teff7500_g3.5_v100.fits	0.807	-37.874
	teff7500_g3.5_v200.fits	0.795	-40.181
March 23, 2008	teff7500_g3.5_v10.fits	0.594	-39.030
	teff7500_g3.5_v100.fits	0.795	-40.010
	teff7500_g3.5_v200.fits	0.782	-42.521

[1]The model names are constructed as follows: 't09000' or 'teff9000' = T_{eff} of 9000 K, 'g40' or '_g4.0' = log(g) of 4.0, 'v2r10' or 'v10' = 10 kms^{-1} project rotational velocity

Table 7. Ca II 3968 Å Comparison

	Wavelength, Å	Equiv. Wid.	Error in Equiv. Wid.	log(N_a)	Error in log(N_a)
HD 158352 (21 March 2008)	3967.77	0.01446	0.00190	11.182	0.057
HD 158352 (22 March 2008)	3967.79	0.00634	0.00186	10.824	0.128
HD 158352 (23 March 2008)	3967.79	0.01184	0.00198	11.095	0.073
HD 158737 (21 March 2008)	3967.77	0.00511	0.00190	10.730	0.162

Table 8. Ca II 3932 Å Comparison

	Wavelength, Å	Equiv. Wid.	Error in Equiv. Wid.	log(N_a)	Error in log(N_a)
HD 158352 (21 March 2008)	3932.96	0.04180	0.00144	11.351	0.015
HD 158352 (22 March 2008)	3932.95	0.02372	0.00174	11.105	0.032
HD 158352 (23 March 2008)	3932.96	0.03754	0.00171	11.304	0.020
HD 158737 (21 March 2008)	3932.96	0.01515	0.00123	10.910	0.035

Table 9. Abundance Measurements, HD 158352

Object (Date)	Wavelength, Å	Equiv. Wid.	Error in Equiv. Wid.	$\log(N_a)$	Error in $\log(N_a)$
Na I 5888					
158352 (21 March 2008)	5888.91	0.02585	0.00133	10.808	0.02235
158352 (22 March 2008)	5888.94	0.01617	0.00155	10.605	0.04158
158352 (23 March 2008)	5888.89	0.02647	0.00156	10.819	0.02558
158737 (21 March 2008)	5888.91	0.02527	0.00110	10.799	0.01895
157089 (21 March 2008)	5888.94	0.01531	0.00076	10.581	0.02159
Na I 5894					
158352 (21 March 2008)	5894.88	0.01962	0.00126	10.989	0.02796
158352 (22 March 2008)	5894.92	0.00974	0.00146	10.684	0.06495
158352 (23 March 2008)	5894.91	0.01541	0.00146	10.884	0.04113
158737 (21 March 2008)	5894.88	0.01699	0.00111	10.926	0.02848
157089 (21 March 2008)	5894.91	0.00424	0.00077	10.324	0.07896

Table 10. Observations

ID	Other	RA	Dec	Spec Type	B (mag)	V (mag)	δ (deg)	Dist (pc)	Dates Obs	Obs
HD21620		03 : 31 : 29.34	+49 : 12 : 35.17	A0Vn	6.350	6.287	0.0000	143	071122	McDonald
HD21375		03 : 28 : 53.65	+49 : 04 : 13.17	A1V	7.580	7.470	0.4470	171	···	···
HD21428		03 : 29 : 22.05	+49 : 30 : 32.21	B3V	4.578	4.678	0.4570	171	071122	McDonald
HD21600		03 : 31 : 14.68	+49 : 42 : 22.46	A6Vn	8.790	7.640	0.4980	147	···	···
HIP16455		03 : 31 : 58.72	+49 : 52 : 12.57	F1V	9.580	9.250	0.6650	141	071122	McDonald
HD21844		03 : 33 : 20.97	+47 : 57 : 00.30	F0	7.100	6.700	1.2970	94	···	···
HD24863		03 : 54 : 33.96	−52 : 41 : 25.53	A4V	6.615	6.472	0.0000	107	071024	LCO
									071025	LCO
									071026	LCO
									071027	LCO
HD25061		03 : 56 : 25.30	−52 : 55 : 51.12	K1V	10.110	9.260	0.3700	56	071025	LCO
HD24977		03 : 55 : 40.02	−51 : 47 : 56.64	F2V	8.100	7.820	0.9100	127	071025	LCO
HD25913		04 : 03 : 40.56	−52 : 55 : 44.23	F0IV	7.900	7.400	1.4000	83	071025	LCO
HD25448		03 : 59 : 54.17	−54 : 09 : 40.18	F5V	8.190	7.810	1.6700	104	071025	LCO
HD24905		03 : 54 : 51.80	−54 : 26 : 52.35	G0V	9.140	8.570	1.7600	129	071025	LCO
HD39283	ζ Aur	05 : 54 : 50.78	+55 : 42 : 25.01	A2V	5.019	4.968	0.0000	74	071120	McDonald
HD40062		05 : 59 : 45.83	+55 : 19 : 15.09	A5m	6.710	6.410	0.7960	105	071121	McDonald
HD38091		05 : 46 : 30.39	+56 : 06 : 56.07	A4Vn	6.080	5.931	1.2380	59	071121	McDonald
HD37282		05 : 40 : 35.08	+55 : 05 : 56.85	F2	8.480	8.100	2.1130	79	···	···
HD37030		05 : 38 : 48.52	+55 : 44 : 52.69	F5	8.340	7.900	2.2580	62	···	···
HD233165		05 : 48 : 29.72	+52 : 32 : 38.43	G0	9.690	9.180	3.2970	94	···	···
HD42111		06 : 08 : 57.90	+02 : 29 : 58.89	A3Vn	5.739	5.673	0.0000	187	071024	LCO
									071025	LCO
									071027	LCO
HD42092		06 : 08 : 59.68	+02 : 29 : 47.03	A0	6.900	6.850	0.0081	170	071024	LCO
HD42256		06 : 09 : 49.14	+02 : 52 : 10.09	K0	7.400	6.600	0.4270	154	071024	LCO
HD41715		06 : 06 : 54.73	+02 : 10 : 23.03	A0	7.300	7.700	0.6079	204	071024	LCO
HD43021		06 : 14 : 10.42	+02 : 34 : 28.63	A0	8.010	7.840	1.3030	127	071025	LCO
HD40512		05 : 59 : 29.92	+02 : 28 : 34.17	F5IV	8.180	7.750	2.3650	67	071025	LCO
HD50241	α Pic	06 : 48 : 11.45	−61 : 56 : 29.01	A7IV	3.465	3.253	0.0000	30	070310	LCO
									070310	LCO
									070311	LCO
									070311	LCO
									071024	LCO
									071025	LCO
									071027	LCO
									080321	LCO
									080322	LCO
									080323	LCO
HD49035		06 : 42 : 23.25	−61 : 13 : 29.88	G5/G6IV/V	9.260	8.530	0.9945	54	070310	LCO
									070311	LCO
									071024	LCO
HD53143		06 : 59 : 59.66	−61 : 20 : 10.26	K1V	7.610	6.810	1.5270	18	070310	LCO
									070311	LCO
									071024	LCO

Table 10—Continued

ID	Other	RA	Dec	Spec Type	B (mag)	V (mag)	δ (deg)	Dist (pc)	Dates Obs	Obs
HD48115		06 : 38 : 00.50	−59 : 46 : 24.37	G0V	9.340	8.790	2.4970	57	070310	LCO
									070311	LCO
									071024	LCO
HD56533		07 : 13 : 07.09	−63 : 20 : 41.80	K5V	10.360	9.800	3.1890	20	070310	LCO
									070311	LCO
HD77190	67 Cnc	09 : 01 : 48.839	+27 : 54 : 09.34	A8Vn	6.284	6.064	0.0000	59	070310	LCO
									070310	LCO
									070311	LCO
BD+281673		09 : 01 : 44.777	+27 : 55 : 37.86	K7	10.350	9.080	0.0288	···	070311	LCO
HD76332		08 : 56 : 22.937	+28 : 40 : 04.58	G2V	9.200	8.580	1.4200	54	070311	LCO
HD78277		09 : 08 : 02.743	+27 : 33 : 32.47	G2IV	8.820	8.190	1.4210	92	070311	LCO
HIP44858		09 : 08 : 23.870	+27 : 32 : 07.57	G0V	8.760	8.260	1.5030	48	070311	LCO
HD78251		09 : 07 : 53.205	+25 : 37 : 34.66	A0	7.230	7.040	2.6490	94	070311	LCO
HD98353	55 Uma	11 : 19 : 07.90	+38 : 11 : 08.00	A2V	4.900	4.800	0.0000	56	···	···
HD98423		11 : 19 : 41.50	+38 : 06 : 03.16	F2	7.700	7.200	0.1390	57	···	···
HD99579		11 : 27 : 44.77	+37 : 56 : 17.49	F8	7.798	7.282	1.7140	78	···	···
HD99787		11 : 29 : 04.12	+39 : 20 : 13.11	A2V	5.373	5.354	2.2530	64	···	···
HD98186		11 : 18 : 00.48	+35 : 26 : 41.81	G5	9.040	8.280	2.7500	37	···	···
HD100360		11 : 33 : 13.41	+38 : 51 : 26.49	K0	8.480	7.830	2.8370	51	···	···
HD118232	24 Cvn	13 : 34 : 27.26	+49 : 00 : 57.50	A5V	4.820	4.700	0.0000	58	···	···
HD117963		13 : 32 : 51.52	+49 : 08 : 24.26	G0	8.800	8.100	0.2890	78	···	···
HIP66589		13 : 39 : 00.03	+49 : 21 : 56.53	K5	11.670	10.630	0.8220	82	···	···
HIP66262		13 : 34 : 49.80	+47 : 22 : 34.35	K5	11.340	10.230	1.6410	44	···	···
HIP66804		13 : 41 : 37.20	+46 : 55 : 07.77	G5	10.310	9.560	2.4160	62	···	···
HIP66315		13 : 35 : 29.16	+46 : 33 : 30.91	K3	11.980	10.890	2.4620	42	···	···
HD142926	4 Her	15 : 55 : 30.59	+42 : 33 : 58.30	B9pe	5.640	5.740	0.0000	148	···	···
HD143208		15 : 57 : 26.90	+41 : 39 : 42.83	F5	9.600	8.900	0.9730	136	···	···
HD144207		16 : 02 : 51.23	+43 : 02 : 23.17	F2	9.420	8.980	1.4280	172	···	···
HIP78640		16 : 03 : 13.30	+42 : 14 : 46.65	F5	10.330	9.850	1.4590	125	···	···
HD141347		15 : 47 : 02.14	+41 : 43 : 11.00	F2	8.560	8.160	1.7840	166	···	···
HD143722		16 : 00 : 11.83	+44 : 16 : 46.22	K0	7.956	6.785	1.9130	142	···	···
HD148283	25 Her	16 : 25 : 24.17	+37 : 23 : 38.69	A5V	5.698	5.537	0.0000	79	···	···
HIP80258		16 : 23 : 04.89	+36 : 50 : 31.48	K3	11.610	10.730	0.7200	69	···	···
HD149058		16 : 30 : 43.82	+37 : 31 : 35.04	G0	8.910	8.440	1.0650	95	···	···
HD149026		16 : 30 : 29.62	+38 : 20 : 50.32	G0	8.720	8.160	1.3850	79	···	···
HD149504		16 : 33 : 41.82	+38 : 05 : 27.83	F5	6.984	6.586	1.7820	56	···	···
HIP80271		16 : 23 : 09.18	+35 : 35 : 18.32	F8	9.840	9.290	1.8610	95	···	···
HD158352		17 : 28 : 49.655	+00 : 19 : 50.25	A8V	5.639	5.424	0.0000	63	080321	LCO
									080322	LCO
									080323	LCO
BD+003696		17 : 28 : 47.390	+00 : 20 : 24.27	G5	11.000	9.600	0.0134	···	080321	LCO
HIP85416		17 : 27 : 16.222	−00 : 15 : 11.06	G5	10.330	9.560	0.7012	60	···	···
HD158737		17 : 30 : 51.526	+01 : 07 : 10.39	F0	7.300	7.000	0.9393	71	080321	LCO
HD157089		17 : 21 : 07.056	+01 : 26 : 34.98	F9V	7.550	6.950	2.2250	39	080321	LCO
HD159357		17 : 34 : 29.412	−01 : 45 : 38.07	F8	8.300	7.900	2.5250	73	···	···

Table 10—Continued

ID	Other	RA	Dec	Spec Type	B (mag)	V (mag)	δ (deg)	Dist (pc)	Dates Obs	Obs
HD196724	29 Vul	20 : 38 : 31.34	+21 : 12 : 04.23	A0V	4.800	4.820	0.0000	65	071024	LCO
									071025	LCO
									071026	LCO
HD197396		20 : 42 : 49.36	+20 : 50 : 40.61	K0	9.200	8.400	1.0700	25	071024	LCO
HD197076		20 : 40 : 45.14	+19 : 56 : 07.93	G5V	7.080	6.450	1.3700	21	071024	LCO
HD347427		20 : 44 : 13.02	+21 : 54 : 26.73	K2	10.850	10.090	1.5000	82	···	···
HD198135		20 : 47 : 40.92	+22 : 41 : 44.83	F8	8.010	7.630	2.6000	78	071024	LCO
HD352975		20 : 45 : 42.31	+19 : 07 : 31.62	G5	10.630	9.860	2.6700	64	071025	LCO
HD199603		20 : 58 : 41.84	−14 : 28 : 59.26	A9V	6.180	5.959	0.0000	85	071024	LCO
HD199505		20 : 58 : 04.37	−15 : 09 : 42.67	G4V	9.190	8.600	0.7000	81	071024	LCO
									071025	LCO
									071026	LCO
HD199828		20 : 59 : 54.83	−13 : 03 : 05.88	A3IV	6.775	6.617	1.4600	98	071024	LCO
HD199706		20 : 59 : 27.71	−16 : 52 : 46.56	F4V	8.380	7.990	2.4000	92	071024	LCO
HD201462		21 : 10 : 08.03	−15 : 42 : 13.29	F0V	7.700	7.400	3.0200	101	071024	LCO
HD358328		21 : 10 : 02.22	−13 : 10 : 35.36	K5V	11.690	10.580	3.0500	45	···	···
HD217782	2 And	23 : 02 : 36.38	+42 : 45 : 28.06	A3Vn	5.180	5.093	0.0000	107	071120	McDonald
HD217799		23 : 02 : 43.62	+41 : 16 : 41.69	G5	8.480	7.603	1.4790	105	···	···
HIP114299		23 : 08 : 55.12	+43 : 52 : 14.21	F2	9.530	9.160	1.5990	104	071121	McDonald
HD217731		23 : 02 : 11.33	+44 : 34 : 22.29	K0	7.373	6.427	1.8170	110	071121	McDonald
HD216854		22 : 55 : 56.77	+41 : 20 : 06.15	F5	7.810	7.320	1.8850	102	···	···
HD219307		23 : 14 : 23.26	+43 : 28 : 33.74	F2	8.530	8.160	2.2660	116	···	···
HD223884		23 : 53 : 20.84	−24 : 13 : 45.33	A5V	6.407	6.235	0.0000	92	071024	LCO
									071025	LCO
									071026	LCO
HD223490		23 : 49 : 57.65	−24 : 09 : 56.76	F4V	9.110	8.680	0.7800	98	071024	LCO
HD223366		23 : 48 : 56.93	−25 : 08 : 40.95	G5V	10.340	9.750	1.3600	90	···	···
HD224746		00 : 00 : 18.33	−23 : 27 : 09.70	G0V	9.530	9.050	1.7700	103	071024	LCO
HD223243		23 : 47 : 53.16	−22 : 36 : 32.37	F4V	9.010	8.590	2.0500	97	071024	LCO
HD225076		00 : 03 : 10.72	−24 : 35 : 17.73	F3V	8.340	7.970	2.2700	84	071024	LCO
HD224463		23 : 58 : 08.55	−33 : 07 : 55.74	F2V	9.520	9.150	0.0000	108	071025	LCO
									071026	LCO
									071027	LCO
HD224410		23 : 57 : 38.35	−33 : 11 : 20.80	F6V	7.475	7.025	0.2000	68	071025	LCO
HD224886		00 : 01 : 30.08	−33 : 47 : 33.98	F3V	8.980	8.600	0.9600	121	071025	LCO
HD224007		23 : 54 : 28.96	−32 : 28 : 18.54	F7V	9.380	8.900	1.0100	82	071025	LCO
HD224863		00 : 01 : 18.39	−31 : 53 : 58.63	F7V	9.840	9.350	1.4000	123	071025	LCO
HD224642		23 : 59 : 34.61	−31 : 41 : 17.79	F2V	7.873	7.551	1.4800	118	071025	LCO